

Investigations in Scramjet Mixing Enhancement Using Richtmyer-Meshkov Instabilities

Alex Shepherd
Carleton University

May 30, 2023

Abstract

This report investigates shock-wave induced mixing enhancement in hypersonic air-breathing engines, or scramjets. The scramjet combustor design studied by Yang et al. [6] through numerical and physical experiments is recreated in this report using CFD. In this design, a pair of transverse high temperature jets (THTJ) are used to promote mixing downstream by inducing Richtmyer-Meshkov instabilities (RMI). Results from the original study were unable to be reproduced for the chemically reacting case, frozen results were obtained which demonstrate increased mixing via RMI. OpenFOAM is used in this report with the third-party solver hy2Foam which was modified to include turbulent terms. Verification and validation studies are preformed, so a secondary objective is to assess these modifications.

Chapter 1

Introduction

The science fiction author Robert Heinlein once said "Once you get to Earth orbit, you're halfway to anywhere." True in the literal sense? Maybe not. Nevertheless, this quote is still insightful. Easier access to orbit will enable the faster development of space technologies, since it is difficult to develop for an environment which is only available to visit a few times a year. Despite their power output, current launch vehicles, using chemical rockets, consist of mostly propellant, are expensive and inefficient, all contributing to their infrequent use. In the decades since the first voyage beyond our atmosphere, numerous technological and scientific advances have been made in the realm of space flight. And yet, the modern day rocket Atlas V HLV still needs to devote 92% of its total mass to propellant [1] in order to reach orbit. It is clear something needs to be radically changed to make everyday affordable space flight a reality.

Efficiency for a propulsive engine can loosely be characterized by specific impulse:

$$I_{sp} = \frac{F_{thrust}}{g \dot{m}} \quad (1.1)$$

where F_{thrust} is the force produced, \dot{m} is the mass flow rate and g is the gravitational acceleration [2]. Specific impulses for various propulsion methods are shown in figure 1.1, showing that conventional rockets have the lowest propulsive efficiencies of the engines shown, however their ability to work in the vacuum of space make them a necessity. The Breguet range equation is:

$$R = V I_{sp} \frac{L}{D} \ln \left(\frac{m_0}{m_f} \right) \quad (1.2)$$

where the aircraft range is R , its cruise velocity V , the lift to drag ratio L/D and the ratio of initial to final vehicle mass m_0/m_f [2]. While this equation only applies to flights at cruising velocities, it serves to demonstrate the exponential relation between mass fraction and specific impulse. Hydrocarbon fuels are commonly considered by designs despite having a lower specific impulse due to their ease of storage, in contrast to liquid hydrogen which must be stored at cryogenic temperatures, and the widespread use by civilian and military industries.

Rocket efficiency is outmatched by the air-breathing options, though its consistent performance over all speed ranges and altitudes make it the engine of choice for modern day launch vehicles. Referring to figure 1.1, the specific impulse of air-breathing engines is more than double that of rockets, though the need for different engine types, as opposed to an all rocket design. However, covering the whole range of speeds and altitudes would normally require a multistage vehicle. One method to avoid this is to use combined cycle propulsion in which two or more engine types are integrated to create a more versatile system [2]. These can be divided into roughly two categories, turbine (TBCC) and rocket based (RBCC) combined cycles, the former extending turbines to high supersonic speeds and scramjets to trans-atmospheric flight for the latter. One design for a TBCC combines turbojets and rockets makes use of cryogenically stored liquid hydrogen rocket fuel to cool incoming air to subsonic speeds and an example of RBCC uses a fuel injector that doubles as a rocket [2].

All engines, except rockets, listed in figure 1.1 can be broadly analyzed by the Brayton thermodynamic cycle, characterized by compression, combustion, expansion and heat rejection, or exhaust, into atmosphere

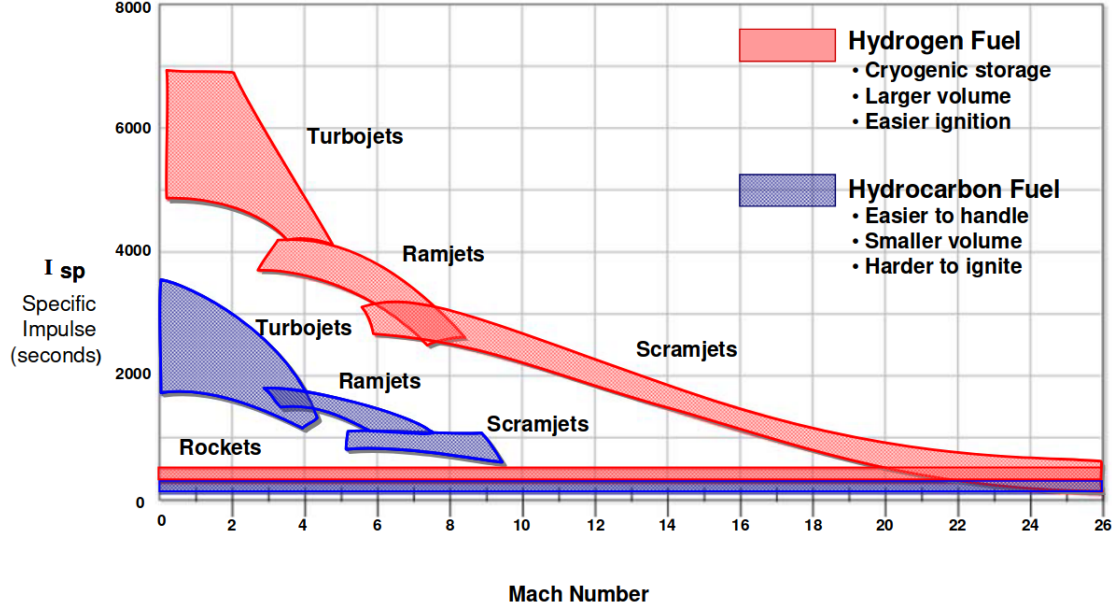


Figure 1.1: Engine performance characteristics. Reproduced from Tang and Chase [3].

[2]. While these cycles are not very effective in the way of design, they are good for the purposes of preliminary analyses and conceptual understanding. In this ideal thermodynamic cycle, compression and expansion steps are isentropic while combustion and exhaust are isobaric. In turbojets, and gas turbines in general, the compression and expansion steps require an active compressor and turbine, whereas ramjets and scramjets require no moving parts and use shock waves to fulfill this need. The difference between these engines is that combustion occurs at subsonic speeds for ramjets and supersonically in scramjets, hence the name supersonic combustor ramjet.

In their review of reusable launch vehicle (RLV) concepts, Mankins [4] compares combined-cycle propulsion proposals to a baseline, single stage to orbit O_2-H_2 rocket with a propellant fraction of 0.89, assuming near ideal performance. The joint NASA-US Air Force national aerospace plane (NASP) study suggests propellant fractions of around 0.70, using air-breathing engines until Mach 25 where rockets are then used till orbit. Both baseline and NASP designs have tight performance margins, something that will not help lower costs, and have lifetimes of only 200 flights. Another proposal by the Kaiser-Marquardt corporation, on the other hand, opts a larger propellant mass fraction of 0.78 with lifetimes of 1000–2000 flights and larger margins, increasing versatility. In either case, Mankins study [4] shows that the integration of air-breathing propulsion into space launch vehicles is necessary to make this drastic change.

Besides higher payload fractions, conventional aircraft are far more reliable and flexible in their mission profiles than rockets, which are confined to only a handful of launch sites and windows. As analyzed by Flaherty et al. [5], introducing air breathing engines to launch vehicles can significantly increase mission flexibility, some authors even suggest better safety and reliability. To evaluate these operability benefits, Flaherty et al. [5] compared all rocket and RBCC vehicles, designed with similar mission profiles in mind, launching into an orbital rendezvous trajectory using Monte-Carlo simulations. The study found that launch windows for the RBCC vehicle were 4.5 min on average with around 4 launch opportunities per day compared to 1 min and 2 opportunities for the all rocket system. Air-breathing launch vehicles can cruise at hypersonic speeds before committing to an orbital, or suborbital, trajectory, a more flexible option than having to select the nearest ground launch site and perform expensive orbital manoeuvres later.

Unlike rocketry, which has had the privilege of industry and academic development over the past half century, scramjets are still an emerging technology that require a lot of research and development to put into practice. One area of study is fuel mixing at supersonic speeds, or how to properly mix fuel and air where the fluid residence times are on the order of milliseconds, which present its own unique challenges. Using the Blasius flat plate solution to illustrate this point, the boundary layer thickness is proportional to

$1/\sqrt{U}$ where U is the free-stream velocity meaning it decreases with speed. This report seeks to recreate the experiment of Yang et al. [6] who numerically simulated the combustor section of a kerosene fuelled scramjet using shock induced instabilities to increase mixing. Results from this study were also confirmed by Yang et al. [6] in wind tunnel testing. This report also seeks to contribute to existing CFD tools, adding to their ability to simulate supersonic turbulent reacting flow.

Chapter 2

Literature Review

Mixing is almost synonymous with turbulence, laminar flow would be subject to slow molecular diffusion, so it should come as no surprise that techniques to promote mixing are almost identical to those for turbulence. Vorticity, defined as $\boldsymbol{\Omega} = \nabla \times \mathbf{u}$ where \mathbf{u} is the velocity, is a common quantity to characterize the amount of turbulence and can be thought of as angular momentum of the fluid. Its transport is given by:

$$\frac{D\boldsymbol{\Omega}}{Dt} = \boldsymbol{\Omega} \cdot \mathbf{S} - \boldsymbol{\Omega} \nabla \cdot \mathbf{u} + \frac{1}{\rho^2} \nabla \rho \times \nabla p + \nabla \times \frac{\nabla \cdot \boldsymbol{\tau}}{\rho} \quad (2.1)$$

where

ρ Density

p Pressure

$\boldsymbol{\tau}$ Stress tensor

\mathbf{S} Strain tensor

Equation (2.1) describes vorticity generation through deformation and dilation due to the strain tensor, misalignment of pressure and density gradients and those due to viscous effects. Known as baroclinic torque, the misalignment of pressure and density gradients is a uniquely compressible effect and is something sought after in supersonic mixing techniques [7]. A common example of this misalignment in scramjets is when the fuel injector plume interacts with a shock wave [8], density gradients that would otherwise be normal to the shock would have a tangential component.

Three basic mechanisms are at play for fluid mixing: Kelvin-Helmoltz (KH), Rayleigh-Taylor (RT) and Richtmyer-Meshkov (RMI) instabilities [9]. KH instabilities arise in the shear layers between two fluids of different velocity, and has been directly observed in supersonic flow [7]. RM and RT instabilities exist between fluids of different densities under acceleration, however the RMI occurs in shock waves, characterized by impulsive rather than steady acceleration. The RMI was first analyzed by Richtmyer who proposed that for an intermediate time period, long enough for transmitted and reflected shocks to travel far away but can still be described by linear theory, the fluid interface can be treated as incompressible [10]. For this intermediate period, Richtmyer used the linear perturbation theory of Taylor and assumed an impulsive acceleration, finding that growth rate is constant in time and proportional to the Atwood number, relative densities between the fluids. Initial experiments with strong shocks seem to support Richtmyer's impulsive model, however studies investigating weak shocks showed growth rate to be configuration dependant, whether the shock wave travels into the heavy or light fluid. Later work derived more accurate analytical solutions using linear compressible theory that are configuration dependent [10]. These solutions also correctly predict interface growth between fluids of different heat capacity ratios despite having the same density, showing that the RMI is a distinct phenomenon than the RT instability.

In their review paper, Tan et al. [7] classifies passive mixing enhancement into two groups: those with the goal of promoting instabilities along the wall and those producing large scale structures. The former method usually involves disturbances in a splitter plate, such as small triangular extrusions, to destabilize the shear layer. However, more research has been done with techniques that promote large structures, struts,

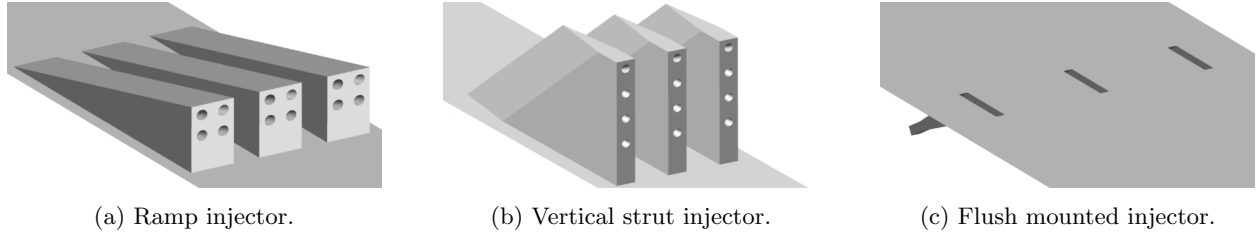


Figure 2.1: Fuel injector types as studied by Shenoy et al. [8].

tabs, and other protrusions into the flow. Ramps generally induce stream-wise vorticities by having the main flow spill over onto the sides while the wave-like cross-section of lobbed mixers interlace the flows on either side of the splitting plate. A technique also seen in subsonic mixers, Flesberg et al. [11] investigate dual wall mounted swirled fuel injector jets, varying their core size, spacing and spin orientations, co- or counter-rotating flow. This study found that counter-rotating flows, spinning towards each other near the wall, that were separated by five jet radii increased turbulent kinetic energy the most. Fuel injector nozzle geometry has also been studied, considering asymmetric and notched designs [7].

Fuel injector mounting is another area of research and can typically be classified as strut, ramp and flush mounted injectors as depicted in figure 2.1. Not constrained to the walls, strut injectors can be placed directly in the flow wherever fuel is needed and are generally oriented in the stream-wise direction which reduces back pressure [8]. These struts are designed to be slender so as not to obstruct the main flow, which in turn raises structural and cooling concerns. The experiment of Yang et al. [6] used a strut injector actively cooled by liquid fuel to mitigate this. Ramp injectors are confined to the walls where active cooling and structural integrity is not as much of a concern but have less potential for mixing [8]. As they are hidden from the stream, flush mounted injectors produce the least amount of back pressure, this also means that additional structures are needed to induce oblique shocks, key to generating baroclinic torque. Studies have shown that jet penetration for flush mounted injectors is proportional to the dynamic pressure ratio between the two streams, suggesting that these become less efficient at higher Mach numbers. This conjecture is supported by Shenoy et al. [8] who compared these injector types at different flight conditions and found that strut injectors had the best mixing efficiency at Mach 12 and 15 whereas flush mounted injectors had the best efficiency at Mach 8.

Unlike passive methods, active mixing enhancement requires external power input and control to function, and will only be mentioned here briefly. Among these methods are osculating flaps mounted and oriented normal to the wall, which have been found to increase boundary layer growth by 50%, oscillating at 20 kHz, compared to a smooth wall [7]. Another study investigated mounting the flaps to a splitter plate, oriented in the stream-wise direction, and saw over double the increase from wall mounted flaps. Other methods that have been studied are electromagnetic excitation, such as glow discharge, pulsed injection and acoustic excitation, all of which require fine-tuning to reach optimum efficiency. Counterflows have also been studied, where a thin ring around the fuel injector provides suction, resulting in an inflection point in the velocity profile. These have also been shown to increase mixing significantly with minimal suction of the main flow. Except possibly counterflows, which only modify the fuel injectors, introducing active methods removes a benefit of ramjets and scramjets, that of no moving parts, which will require more maintenance and may introduce unnecessary complexity.

Chapter 3

Governing Equations

The Knudsen number for a gas is the ratio of free mean path length ℓ to the length scale L :

$$\text{Kn} = \frac{\ell}{L} \quad (3.1)$$

and, if $\text{Kn} \ll 1$, the continuum hypothesis holds [12]. Under this assumption, the governing equations are [13]:

$$\frac{\partial \rho}{\partial t} + \frac{\partial}{\partial x_j}(\rho u_j) = 0 \quad (3.2)$$

$$\frac{\partial \rho u_i}{\partial t} + \frac{\partial}{\partial x_j}(\rho u_i u_j) = \frac{\partial}{\partial x_j}(\tau_{ij} - \delta_{ij} p) \quad (3.3)$$

$$\frac{\partial \rho E}{\partial t} + \frac{\partial}{\partial x_j}(\rho H u_j) = \frac{\partial}{\partial x_j}(\tau_{ij} u_i - q_j) \quad (3.4)$$

$$\frac{\partial \rho Y_s}{\partial t} + \frac{\partial}{\partial x_j}(\rho u_j Y_s) = \dot{\omega}_s + \frac{\partial}{\partial x_j} \left(\rho D_s \frac{\partial Y_s}{\partial x_j} \right) \quad (3.5)$$

where:

- ρ Density
- u_i Velocity component
- p Pressure
- τ_{ij} Stress tensor
- E Specific total energy
- H Specific total enthalpy
- q_j Heat flux
- D_s Diffusion coefficient
- Y_s Mass fraction
- $\dot{\omega}_s$ Mass production

and subscript s indicates a species specific quantity. These equations are, in order of appearance, the conservation of mass, momentum and energy, with additional mass balance equations for each component of a multispecies mixture.

Assuming heat conduction obeys Fourier's law and radiative transfer is negligible, the heat flux can be written as:

$$q_j = -\kappa \frac{\partial T}{\partial x_j} - \rho D_s h_s \frac{\partial Y_s}{\partial x_j} \quad (3.6)$$

where T is temperature, κ is the thermal conductivity and h_s is the species specific enthalpy. This report also assumes all gases obey the ideal gas law:

$$p = R_s \rho T \quad (3.7)$$

where R_s is the specific gas constant, and Newtonian shear stress:

$$\tau_{ij} = \mu \left(\frac{\partial u_i}{\partial x_j} + \frac{\partial u_j}{\partial x_i} \right) + \lambda \delta_{ij} \frac{\partial u_k}{\partial x_k} \quad (3.8)$$

$$\lambda = -\frac{2}{3}\mu \quad (3.9)$$

where μ and λ are the coefficients of viscosity and bulk viscosity, respectively, with Stoke's hypothesis being used to constrain the latter [12]. Diffusion coefficients are calculated assuming a constant Lewis number, Le , defined as:

$$Le = \frac{\rho D_s c_{p,s}}{\kappa_s} \quad (3.10)$$

representing the ratio of mass to thermal diffusion, and is assumed to be 1.4, a typical value given for air [14]. Occasionally the Schmidt number Sc , viscous to mass diffusion, is given instead and is related to the Lewis number by the Prantl number Pr , viscous to thermal diffusion [12]:

$$Sc = \frac{\mu_s}{\rho D_s} \quad (3.11)$$

$$Pr = \frac{\mu_s c_{p,s}}{\kappa_s} \quad (3.12)$$

$$Le = \frac{Pr}{Sc} \quad (3.13)$$

Other methods of calculating mass diffusion coefficients exist, such as the relations derived from kinetic theory [12], however this report will use constant Lewis number assumption.

Transport quantities, the molecular viscosity and thermal conductivity, are calculated using empirical relations used in NASA's CEA program [15]:

$$\ln \mu = A \ln T + \frac{B}{T} + \frac{C}{T^2} + D \quad (3.14)$$

where $A \dots D$ are empirical constants, μ is the molecular viscosity in μP and T is the temperature in K . Rather than a simple weighted average, mixture properties are better estimated by the more accurate Wilke mixing rule [12]:

$$\mu_{\text{mix}} \approx \sum_i \frac{X_i \mu_i}{\sum_j X_j \phi_{ij}} \quad (3.15)$$

$$\phi_{ij} = \frac{[1 + (\mu_i/\mu_j)^{1/2} (M_j/M_i)^{1/4}]^2}{(8 + 8M_i/M_j)^{1/2}} \quad (3.16)$$

where X_i are mole fractions:

$$X_i = Y_i \frac{M_{\text{mix}}}{M_i} \quad (3.17)$$

Formulas for thermal conductivity are not shown, but can be obtained by substituting μ for κ in the above equations, using units of $\mu\text{W cm}^{-1} \text{K}^{-1}$ in equation (3.14) through (3.16).

3.1 Internal Energy

Specific total energy is the sum of internal (ε) and kinetic energies, related to total enthalpy by:

$$E = \varepsilon + \frac{1}{2}u_i u_i \quad (3.18)$$

$$H = h + \frac{1}{2}u_i u_i = E + \frac{p}{\rho} \quad (3.19)$$

where h is the internal enthalpy, and for a multispecies mixture is a weighted average of its components:

$$\varepsilon = \sum_s Y_s \varepsilon_s \quad (3.20)$$

The internal energy for atoms and molecules, not free electrons, can be further decomposed into translational, rotational, vibrational, electronic and chemical terms [13]:

$$\varepsilon_s = \underbrace{\varepsilon_{s,\text{trans}}}_{\text{translational}} + \underbrace{\varepsilon_{s,\text{rot}}}_{\text{rotational}} + \underbrace{\varepsilon_{s,\text{vib}}}_{\text{vibrational}} + \underbrace{\varepsilon_{s,\text{el}}}_{\text{electronic}} + \underbrace{h_s^\circ}_{\text{chemical}} \quad (3.21)$$

The first three terms of equation (3.21) correspond to the species physical movements, followed by electron energies and chemical potential h_s° , or heat of formation, due to molecular bonds. From statistical mechanics [16], the different energy modes for a gas are given as functions of temperature:

$$\varepsilon_{s,\text{trans}} = \frac{3}{2}R_s T \quad (3.22)$$

$$\varepsilon_{s,\text{rot}} = R_s T \quad (3.23)$$

$$\varepsilon_{s,\text{vib}} = \sum_i g_{i,\text{vib}} \frac{\theta_{i,\text{vib}}/T}{\exp(\theta_{i,\text{vib}}/T) - 1} R_s T \quad (3.24)$$

$$\varepsilon_{s,\text{el}} = \frac{\sum_i g_{i,\text{el}} \theta_{i,\text{el}}/T \exp(-\theta_{i,\text{el}}/T)}{\sum_i g_{i,\text{el}} \exp(-\theta_{i,\text{el}}/T)} R_s T \quad (3.25)$$

where g_i are the number of states per energy level with reference temperature θ_i . The formula for rotational energy, equation (3.23), is given for linear molecules, and has different proportionality constants for monoatomic and non-linear molecules.

Specific enthalpy, used in equation (3.6), is found by:

$$h_s = \varepsilon_s + \frac{p}{\rho} \quad (3.26)$$

Secondary thermodynamic properties can be derived from the specific internal energy:

$$c_{v,s} = \left. \frac{\partial \varepsilon_s}{\partial T} \right|_v \quad (3.27)$$

$$c_{p,s} = c_{v,s} + R_s \quad (3.28)$$

where c_v and c_p are the specific heats at constant volume and pressure, respectively, and are also combined for mixtures using weighted averages:

$$c_v = \sum_s Y_s c_{v,s} \quad (3.29)$$

These can be used to find the heat capacity ratio γ for use in isentropic relations, for example to calculate total temperature and pressure.

3.2 Chemical Modelling

In general, a series of chemical reactions can be written as:

$$\sum_s \nu'_{s,j} X_s \rightleftharpoons \sum_s \nu''_{s,j} X_s \quad (3.30)$$

where $\nu'_{s,j}$ and $\nu''_{s,j}$ are stoichiometric coefficients for reaction j and X denotes the chemical formula for species s [16]. The reaction rate \mathcal{R} and mass production $\dot{\omega}_s$ are:

$$\mathcal{R}_j = k_{f,j} \prod_s [X_s]^{\nu'_{s,j}} - k_{r,j} \prod_s [X_s]^{\nu''_{s,j}} \quad (3.31)$$

$$\dot{\omega}_s = M_s \sum_s (\nu''_{s,j} - \nu'_{s,j}) \mathcal{R}_j \quad (3.32)$$

$$[X_s] = \frac{\rho Y_s}{M_s} \quad (3.33)$$

where $[X_s]$ is the molar concentration, k_f and k_r are the forward and reverse rates, respectively. These chemical rate constants are calculated from the empirical Arrhenius equation:

$$k = AT^\beta \exp\left(\frac{E_a}{RT}\right) \quad (3.34)$$

where R is the universal gas constant, E_a is the activation energy, A and β are experimentally determined constants.

For reversible reactions, the reverse reaction rate can also be calculated from the chemical equilibrium constant K , defined as [17]:

$$K_{c,j} = \frac{\prod_s [X_s]^{\nu''_{s,j}}}{\prod_s [X_s]^{\nu'_{s,j}}} \quad (3.35)$$

$$= \frac{k_{f,j}}{k_{r,j}} \quad (3.36)$$

where subscript c denotes that it is in terms of the concentrations. This constant can also be calculated from the principle of minimizing Gibbs free energy [15]:

$$K_{c,j} = \left(\frac{p_{\text{atm}}}{RT}\right)^{\sum_s \nu''_{s,j} - \nu'_{s,j}} \exp\left(-\sum_s (\nu''_{s,j} - \nu'_{s,j}) \frac{h_s^\circ(T) - s_s^\circ(T)T}{RT}\right) \quad (3.37)$$

where $h^\circ(T)$ and $s^\circ(T)$ are the temperature dependant specie specific enthalpy and entropy measured at standard atmospheric pressure. These can be derived from the thermodynamic partition functions or calculated using the corresponding correlations from Gordon and McBride [18].

3.3 Turbulence Modelling

Putting it simply, turbulence is just random fluctuations at small scales, significantly smaller than the domain geometry, in the fluid flow. And to account for this, quantities are time averaged:

$$\phi(t) = \bar{\phi} + \phi' \quad (3.38)$$

$$\bar{\phi} = \lim_{T \rightarrow \infty} \frac{1}{T} \int_t^{t+T} \phi(t) dt \quad (3.39)$$

where ϕ represents an arbitrary quantity and this process is known as Reynolds averaging [12]. In compressible flow, it is sometimes more useful to consider Favre, or mass weighted, averaging:

$$\phi(t) = \tilde{\phi} + \phi'' \quad (3.40)$$

$$\tilde{\phi} = \frac{1}{\bar{\rho}} \lim_{T \rightarrow \infty} \frac{1}{T} \int_t^{t+T} \rho \phi(t) dt \quad (3.41)$$

Turbulence can be accounted for by Favre averaging the governing equations, 3.2 through 3.5:

$$\frac{\partial \bar{\rho}}{\partial t} + \frac{\partial}{\partial x_j} (\bar{\rho} \tilde{u}_j) = 0 \quad (3.42)$$

$$\frac{\partial \bar{\rho} \tilde{u}_i}{\partial t} + \frac{\partial}{\partial x_j} (\bar{\rho} \tilde{u}_i \tilde{u}_j) = \frac{\partial}{\partial x_j} \left(\bar{\tau}_{ij} - \bar{\rho} \widetilde{u_i'' u_j''} - \delta_{ij} \bar{p} \right) \quad (3.43)$$

$$\frac{\partial \bar{\rho} \tilde{E}}{\partial t} + \frac{\partial}{\partial x_j} (\bar{\rho} \tilde{H} \tilde{u}_j) = \frac{\partial}{\partial x_j} \left(\bar{\tau}_{ij} \tilde{u}_i + \overline{\tau_{ij} u_i''} - \bar{q} - \bar{\rho} \widetilde{H'' u_j''} \right) \quad (3.44)$$

$$\frac{\partial \bar{\rho} \tilde{Y}_s}{\partial t} + \frac{\partial}{\partial x_j} (\bar{\rho} \tilde{u}_j \tilde{Y}_s) = \bar{\omega}_s + \frac{\partial}{\partial x_j} \left(\bar{\rho} D_s \frac{\partial \tilde{Y}_s}{\partial x_j} - \bar{\rho} \widetilde{Y_s'' u_j''} \right) \quad (3.45)$$

Besides the kinetic energy, the Favre averaged total specific enthalpy also accounts for the turbulent kinetic energy k [19]:

$$\tilde{H} = \tilde{h} + \frac{1}{2} \tilde{u}_i \tilde{u}_i + k \quad (3.46)$$

$$H'' = h'' + \tilde{u}_i u_i'' + k'' \quad (3.47)$$

$$k = \frac{1}{2} \widetilde{u_i'' u_i''} \quad (3.48)$$

$$k'' = \frac{1}{2} (u_i'' u_i'')'' \quad (3.49)$$

$$\bar{\rho} \widetilde{H'' u_j''} = \bar{\rho} \widetilde{h'' u_j''} + \bar{\rho} \widetilde{u_i'' u_i'' u_j''} + \bar{\rho} \widetilde{k'' u_j''} \quad (3.50)$$

The Reynolds stress tensor is assumed to follow the Boussinesq hypothesis:

$$\bar{\rho} \widetilde{u_i'' u_j''} = \frac{2}{3} \delta_{ij} \left(\bar{\rho} k + \mu_t \frac{\partial \tilde{u}_k}{\partial x_k} \right) - \mu_t \left(\frac{\partial \tilde{u}_i}{\partial x_j} + \frac{\partial \tilde{u}_j}{\partial x_i} \right) \quad (3.51)$$

where μ_t is the turbulent viscosity. Other approximations made are:

$$\overline{\tau_{ij} u_i''} \approx \mu \frac{\partial k}{\partial x_j} \quad (3.52)$$

$$\bar{\rho} \widetilde{u_j'' h''} = -\frac{\mu_t}{\text{Pr}_t} \frac{\partial \tilde{h}}{\partial x_j} \quad (3.53)$$

$$\bar{\rho} \widetilde{u_j'' k''} = -\frac{\mu_t}{\sigma_k} \frac{\partial k}{\partial x_j} \quad (3.54)$$

$$\bar{\rho} \widetilde{u_j'' Y_s''} = -\frac{\mu_t}{\text{Sc}_t} \frac{\partial \tilde{Y}_s}{\partial x_j} \quad (3.55)$$

where σ_k is a model defined coefficient, Pr_t and Sc_t are turbulent Prandtl and Schmidt numbers, respectively. Like their non-subscripted counterparts, Pr_t and Sc_t signify the ratios of diffusivity, this time for the turbulent instead of molecular diffusion. For simulations with RANS turbulence modelling, Pr_t and Sc_t are usually assumed constant. However, just as how second moment equations can be derived for the Reynolds shear stress, the same can be done for $\bar{\rho} \widetilde{u_j'' Y_s''}$ and $\bar{\rho} \widetilde{u_j'' h''}$ terms. As Baurle [20] points out, this quickly becomes impractical since each species needs at least one additional equation to be solved.

Fluctuations in viscosity, thermal and molecular diffusivities are also assumed negligible:

$$\bar{q} \approx -\bar{\rho} D_s h_s \frac{\partial \tilde{Y}_s}{\partial x_j} - \kappa \frac{\partial \tilde{T}}{\partial x_j} \quad (3.56)$$

$$\bar{\tau}_{ij} \approx \mu \left(\frac{\partial \tilde{u}_i}{\partial x_j} + \frac{\partial \tilde{u}_j}{\partial x_i} \right) - \frac{2}{3} \delta_{ij} \mu \frac{\partial \tilde{u}_k}{\partial x_k} \quad (3.57)$$

RANS turbulence models usually have one or two equations to determine turbulent viscosity, two equation models have transport equations for k and some other turbulent variable and one equation models, like

Spalart-Allmaras, model the turbulent viscosity directly. In order to rectify the need for k in the Boussinesq hypothesis with one equation models, the k terms in the governing equations are dropped [19]. Though turbulent combustion models exist to account for fluctuations in $\bar{\omega}_s$, such as the flamlet model, this report neglects such fluctuations. With these assumptions, the Favre averaged Navier-Stokes equations are, neglecting k terms in the Boussinesq approximation and assuming constant Pr_t and Sc_t :

$$\frac{\partial \bar{\rho}}{\partial t} + \frac{\partial}{\partial x_j}(\bar{\rho} \tilde{u}_j) = 0 \quad (3.58)$$

$$\frac{\partial \bar{\rho} \tilde{u}_i}{\partial t} + \frac{\partial}{\partial x_j}(\bar{\rho} \tilde{u}_i \tilde{u}_j) = \frac{\partial}{\partial x_j} \left((\mu + \mu_t) \left(\frac{\partial \tilde{u}_i}{\partial x_j} + \frac{\partial \tilde{u}_j}{\partial x_i} - \frac{2}{3} \delta_{ij} \frac{\partial \tilde{u}_k}{\partial x_k} \right) - \delta_{ij} \bar{p} \right) \quad (3.59)$$

$$\begin{aligned} \frac{\partial \bar{\rho} \tilde{E}}{\partial t} + \frac{\partial}{\partial x_j}(\bar{\rho} \tilde{H} \tilde{u}_j) &= \frac{\partial}{\partial x_j} \left((\mu + \mu_t) \tilde{u}_i \left(\frac{\partial \tilde{u}_i}{\partial x_j} + \frac{\partial \tilde{u}_j}{\partial x_i} - \frac{2}{3} \delta_{ij} \frac{\partial \tilde{u}_k}{\partial x_k} \right) \right. \\ &\quad \left. + \bar{\rho} D_s h_s \frac{\partial \tilde{Y}_s}{\partial x_j} + \left(\frac{\mu}{\text{Pr}} + \frac{\mu_t}{\text{Pr}_t} \right) \frac{\partial \tilde{h}}{\partial x_j} \right) \end{aligned} \quad (3.60)$$

$$\frac{\partial \bar{\rho} \tilde{Y}_s}{\partial t} + \frac{\partial}{\partial x_j}(\bar{\rho} \tilde{u}_j \tilde{Y}_s) = \dot{\omega}_s + \frac{\partial}{\partial x_j} \left(\bar{\rho} D_s \frac{\partial \tilde{Y}_s}{\partial x_j} + \frac{\mu_t}{\text{Sc}_t} \frac{\partial \tilde{Y}_s}{\partial x_j} \right) \quad (3.61)$$

This report considers the two equation $k - \omega$ SST model to account for turbulence, where ω is the specific turbulence dissipation rate, chosen for its ability to accurately model a wide range of flows. The $k - \omega$ SST transport equations are:

$$\frac{\partial \bar{\rho} k}{\partial t} + \frac{\partial}{\partial x_j}(\bar{\rho} \tilde{u}_j k) = \mathcal{P} - \beta^* \rho \omega k + \frac{\partial}{\partial x_j} \left((\mu + \sigma_k \mu_t) \frac{\partial k}{\partial x_j} \right) \quad (3.62)$$

$$\frac{\partial \bar{\rho} \omega}{\partial t} + \frac{\partial}{\partial x_j}(\bar{\rho} \tilde{u}_j \omega) = \frac{\bar{\rho} \gamma}{\mu_t} \mathcal{P} - \beta \bar{\rho} \omega^2 + \frac{\partial}{\partial x_j} \left((\mu + \sigma_\omega \mu_t) \frac{\partial \omega}{\partial x_j} \right) + 2(1 - F_1) \frac{\bar{\rho} \sigma_{\omega 2}}{\omega} \frac{\partial k}{\partial x_j} \frac{\partial \omega}{\partial x_j} \quad (3.63)$$

where \mathcal{P} is the production term and Ω_{ij} is the vorticity tensor:

$$\mathcal{P} = \bar{\tau}_{ij} \frac{\partial \tilde{u}_i}{\partial x_j} \quad (3.64)$$

$$\mu_t = \frac{a_1 \bar{\rho} k}{\max(a_1 \omega, \Omega F_2)} \quad (3.65)$$

$$\Omega_{ij} = \frac{1}{2} \left(\frac{\partial \tilde{u}_i}{\partial x_j} - \frac{\partial \tilde{u}_j}{\partial x_i} \right) \quad (3.66)$$

$$\Omega = \sqrt{2 \Omega_{ij} \Omega_{ij}} \quad (3.67)$$

and σ_k , σ_ω , β , β^* , γ and a_1 are model specific constants [21]. Blending functions F_1 and F_2 , elaborated on further by Durbin [22], provide a smooth transition between the free-stream and boundary layer and are nearly constant outside this region.

Chapter 4

Algorithm

As for CFD software, this report makes use of the free and open-source software OpenFOAM, developed by the OpenFOAM foundation [23] and OpenCFD [24] with its development origins in 1996 [25]. OpenFOAM is used primarily for its versatility, many solvers exist to model a variety of flow physics, and open-source nature, it can be freely modified as needed. In particular the Fleming release of hy2Foam solver, part of the hyStrath [26] project, a series of hypersonic and rarefied gas dynamics codes, is used here and was developed in part by the University of Strathclyde, Glasgow. The hy2Foam solver was chosen for its ability to accurately model shock dynamics and reacting flows [13] [27]. As hy2Foam was originally developed for high-altitude external flows, some turbulent terms have not been fully implemented. The solver was modified by the author for this project to include the turbulent terms and can be found here <https://github.com/alexlshepherd/myHy2Foam>.

In the finite volume method, the governing equations are integrated over a control volume and, in particular, the convective terms are discretized as:

$$\int_V \frac{\partial}{\partial x_j} (u_j \Psi) dV \approx \sum_f \Psi_f \phi_f \quad (4.1)$$

where an arbitrary convected quantity Ψ is interpolated onto and summed over the boundary faces f weighted by the volumetric flux ϕ . Face quantities are usually determined by linear interpolation using some weighting coefficient λ that is only a function of geometry. For example, the central differencing scheme is given by:

$$\Psi_f = \lambda \Psi_P + (1 - \lambda) \Psi_N \quad (4.2)$$

$$\lambda = \frac{|\mathbf{S}_f \cdot \mathbf{d}_{fN}|}{|\mathbf{S}_f \cdot \mathbf{d}|} \quad (4.3)$$

where \mathbf{S}_f is the face area vector and \mathbf{d} is the distance vector between cells N and P , depicted in figure 4.1 [28]. Quantities in compressible flows are also transported by wave propagation, and the central scheme of Kurganov and Tadmor accounts for this, modifying discretized convective terms as:

$$\sum_f \Psi_f = \frac{1}{2} \sum_f [\phi_{f+} \Psi_{f+} + \phi_{f-} \Psi_{f-} + \max(\psi_{f+}, \psi_{f-})] \quad (4.4)$$

$$\phi_{f+} = \max(c_{f+} S_f + \psi_{f+}, c_{f-} S_f + \phi_{f-}, 0) \quad (4.5)$$

$$\phi_{f-} = \max(c_{f+} S_f - \psi_{f+}, c_{f-} S_f - \phi_{f-}, 0) \quad (4.6)$$

$$c_{f\pm} = \sqrt{\gamma R T_{f\pm}} \quad (4.7)$$

where f^+ and f^- represent the quantities evaluated on either side of the face. These values are interpolated from the cell centres via total variation diminishing (TVD) flux limiting schemes, such as Minmod, van Leer, and van Albada to name a few. Computation of the gradient is similar to equation (4.4) without the wave propagation term:

$$\int_V \frac{\partial}{\partial x_j} \Psi dV = \frac{1}{2} \sum_f [S_{j,f+} \Psi_{f+} + S_{j,f-} \Psi_{f-}] \quad (4.8)$$

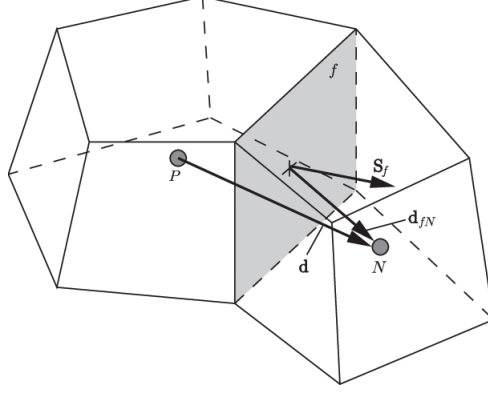


Figure 4.1: Cell discretization. Reproduced from Greenshields et al. [28].

The central methods of Kurganov and Tadmor are implemented by Greenshields et al. [28] in OpenFOAM as a transient semi-implicit solver, named rhoCentralFoam, where explicitly evaluated inviscid equations are corrected by explicit diffusive terms. Conserved variables, mass, momentum $\hat{u}_j = \rho u_j$ and energy density $\hat{E} = \rho E$, are calculated by:

$$\frac{\rho^{n+1} - \rho^n}{\Delta t} + \frac{\partial \hat{u}_j^n}{\partial x_j} = 0 \quad (4.9)$$

$$\frac{(\hat{u}_j)_I^n - \hat{u}_j^n}{\Delta t} + \partial(u_i \hat{u}_j)^n x_i + \frac{\partial p^n}{\partial x_j} = 0 \quad (4.10)$$

$$\frac{\rho^{n+1} u_j^{n+1} - (\hat{u}_j)_I^n}{\Delta t} - \frac{\partial}{\partial x_i} \left(\mu \frac{\partial u_j^{n+1}}{\partial x_i} \right) - \frac{\partial \tau_{\text{exp},ij}}{\partial x_j} = 0 \quad (4.11)$$

$$\frac{\hat{E}_I^n - \hat{E}^n}{\Delta t} + \frac{\partial}{\partial x_j} \left(u_j (\hat{E} + p) \right)^n - \frac{\partial}{\partial x_j} \left(u_i^{n+1} \left(\mu \frac{\partial u_i^{n+1}}{\partial x_j} + \tau_{\text{exp},ij} \right) \right) = 0 \quad (4.12)$$

$$\frac{\rho^{n+1} c_v T^{n+1} - \rho^{n+1} c_v T_I^n}{\Delta t} - \frac{\partial}{\partial x_j} \left(\kappa \frac{\partial T_I^n}{\partial x_j} \right) = 0 \quad (4.13)$$

where superscript n denotes the current time step, subscript I the inviscid predictors and:

$$\tau_{\text{exp},ij} = \mu \frac{\partial u_j^n}{\partial x_i} - \frac{2}{3} \mu \delta_{ij} \frac{\partial u_k^n}{\partial x_k} \quad (4.14)$$

$$T_I^n = \frac{1}{c_v} \left(\frac{\hat{E}_I^n}{\rho^{n+1}} - \frac{1}{2} u_k^{n+1} u_k^{n+1} \right) \quad (4.15)$$

Besides rhoCentralFoam, OpenFOAM also comes prepackaged with rhoPimpleFoam, rhoSimpleFoam and sonicFoam, all of which are single-species compressible flow solvers. As their names suggest, rhoSimpleFoam and rhoPimpleFoam use the pressure based algorithms SIMPLE and PIMPLE, also used by sonicFoam, respectively. Developed with incompressible flows in mind, these algorithms solve the momentum conservation and pressure equations, a rearrangement of the governing equations, and have been extended to include the conservation of energy [29]. As such, density is not a conserved variable in pressure based solvers which is arguably why they are outperformed by rhoCentralFoam in supersonic simulations, see Marcantoni et al. [30] for an in depth evaluation and the comparison in figure 4.2. Pressure based solvers are known to cause spurious oscillators downstream of shockwaves and, in the author's experience, have trouble simulating normal shocks. Specifically rhoPimpleFoam, a transient solver, will slow its march through time as normal shocks begin to develop in certain cases. OpenFOAM comes prepackaged with the reactingFoam solver to model multiphase reacting flow, however it uses the PIMPLE algorithm. The solver hy2Foam was chosen because it is an extension of rhoCentralFoam and, subsequently, uses the central schemes of Kurganov and Tadmor instead of a pressure based algorithm.

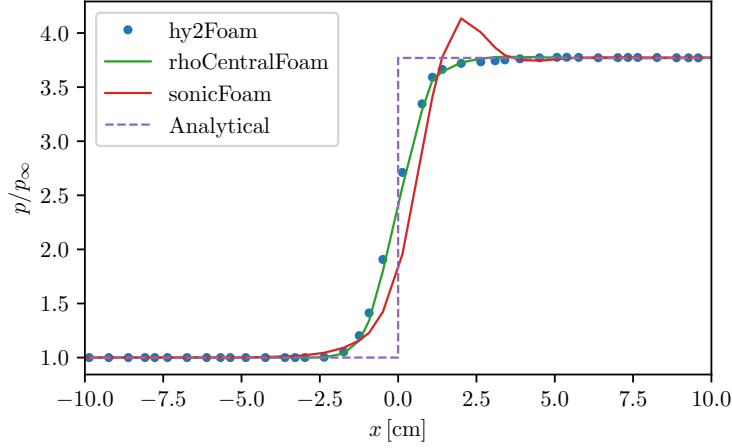


Figure 4.2: Stream-wise pressure distribution showing spurious oscillations in sonicFoam. Flow is air at atmospheric conditions ($p_\infty = 1 \text{ atm}$) and Mach 3 over 20° wedge. Stream-wise distance measured from shock location dictated by analytical solution.

Thompson [31] describes how a series of differential equations, the inviscid Euler equations in particular, can be decomposed according to the system's eigenvalues, resulting in the acoustic approximation. Decomposition of the governing equations allows for the control of incoming and outgoing waves, useful when wave reflections are undesired, such as with an outlet. Poinso and Lele [32] extend this idea to the full Navier-Stokes equations by assuming the contribution of viscous terms to the wave characteristics are negligible. Applied to the discretized boundary of a surface, the local one-dimensional inviscid (LODI) relations can be obtained, shown in figure 4.3, and solving these for the acoustic pressure wave gives:

$$\frac{\partial p}{\partial t} = -\frac{1}{2} (\mathcal{L}_1 + \mathcal{L}_5) \quad (4.16)$$

$$\frac{\partial p}{\partial x_1} = \frac{1}{2} \left(\frac{\mathcal{L}_1}{u_1 - c} + \frac{\mathcal{L}_5}{u_1 + c} \right) \quad (4.17)$$

$$\frac{\partial p}{\partial t} + (u_1 + c) \frac{\partial p}{\partial x_1} = \frac{c}{u_1 - c} \mathcal{L}_1 \quad (4.18)$$

where c is the local speed of sound and subscript 1 denotes the surface normal quantities.

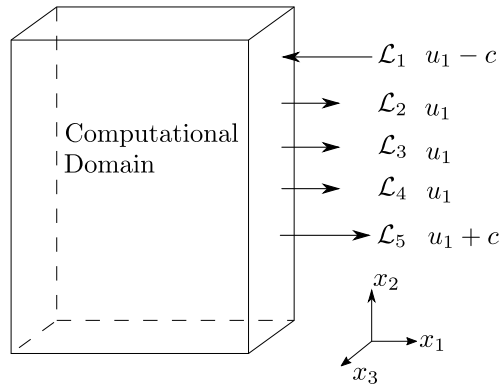


Figure 4.3: Eigenvalue decomposition of Navier-Stokes equations along a cell boundary depicted as acoustic waves into and out of the computational domain.

The most straightforward method to eliminate reflections would be to define $\mathcal{L}_1 = 0$, however Poinso

and Lele [32] find this numerically unstable and opt for a soft boundary instead, allowing some predefined external information to be transmitted inside the computational domain. A subsonic outlet, for example, should still provide information about the far field. Incoming wave amplitude is:

$$\mathcal{L}_1 = K(p - p_\infty) \quad (4.19)$$

$$K = \frac{\sigma(1 - \text{Ma}^2)c}{L} \quad (4.20)$$

where Ma is the Mach number, σ is a constant, L is a characteristic length and p_∞ is the far field pressure. The rationale is that \mathcal{L}_1 will correct the boundary pressure to be the far field value on average, and has been likened to a low pass filter acting on the boundary [33]. This method has behaviour similar to a zero normal stream-wise gradient boundary condition and is used to accelerate convergence.

Chapter 5

Verification and Validation

5.1 Under-Expanded Jet

The use of Richtmyer-Meshkov instabilities to enhance mixing relies heavily on the complex interactions between shock waves and the formation of shock trains. This validation study seeks to isolate this phenomena by simulating the wave patterns formed by an under-expanded supersonic jet, assessing the ability of the CFD algorithm to capture this behaviour. The under-expanded jet was modelled as a cylindrical nozzle ejecting into atmospheric conditions with a total pressure ratio of six, shown with boundary conditions in figure 5.1. Air was used as the fluid, specifying a heat capacity ratio of 1.4, and $k - \omega$ SST as the turbulence model. Of particular importance to this study is the stream-wise distance between the nozzle and the first normal shock. The experimental investigations of Crist et al. [34] found the distance X_j obeys the empirical relation:

$$\frac{X_j}{D} = \sqrt{\frac{p_j}{2.4p_\infty}} \quad (5.1)$$

where D is the inlet diameter, p_j and p_∞ are the total jet and free-stream pressures respectively. With a total pressure ratio of six, equation (5.1) predicts a normalized distance of 1.58.

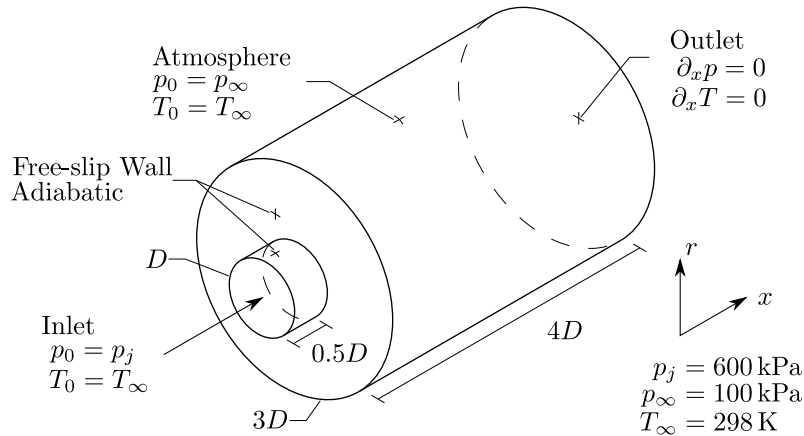


Figure 5.1: Computational domain and boundary conditions for under-expanded jet simulation.

An axisymmetric block structured mesh was used with uniform cell spacing. Grid convergence is demonstrated in figure 5.2, comparing total pressure centre-line profiles for coarse, medium and fine mesh sizes with 10525, 23273 and 42000 cells, which can also be characterized by 50, 75 and 100 cells, respectively, spanning the inlet. Steady state convergence is also demonstrated in appendix B. With convergence demonstrated the fine mesh was used in the subsequent analysis and to produce the artificial Schlieren image in figure 5.3,

showing $X_j/D = 1.53$ as simulated, a difference of 3% from the predicted value of 1.58, obtained from the empirical relation (5.1).

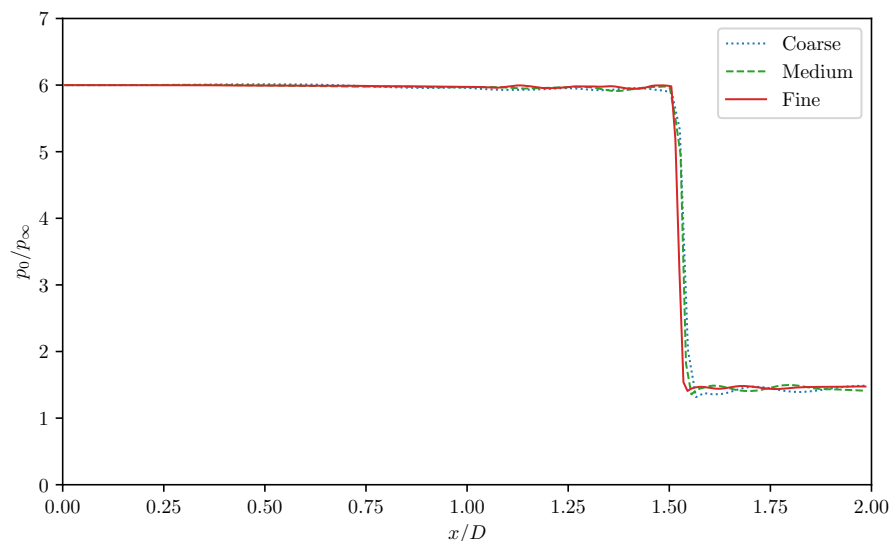


Figure 5.2: Total pressure along centre-line for different mesh sizes with 50 (coarse), 75 (medium) and 100 (fine) cells across the jet diameter. Cell counts are 10525, 23273 and 42000 respectively.

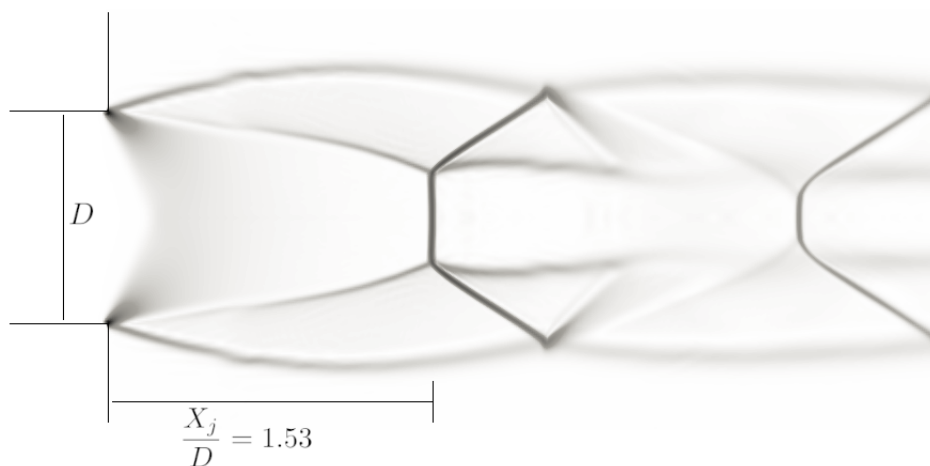


Figure 5.3: Artificial Schlieren of under-expanded jet simulation, showing shock structure and distance to first shock.

Static temperature, pressure and Mach number are taken across the centre-line, normalized by their free-stream values, and plotted in figure 5.4. These quantities are characterized by a steady increase, or decrease, followed by a sharp discontinuity and quickly dissipating numerical oscillations. Ratios between pre- and post-shock values are compared to their theoretical ratios in table 5.1, obtained from normal shock

relations [16]:

$$M_2 = \frac{(\gamma - 1)M_1^2 + 2}{2\gamma M_1^2 - (\gamma - 1)} \quad (5.2)$$

$$\frac{p_2}{p_1} = 1 + \frac{2\gamma}{\gamma + 1}(M_1^2 - 1) \quad (5.3)$$

$$\frac{T_2}{T_1} = \frac{p_2}{p_1} \frac{2 + (\gamma - 1)M_1^2}{(\gamma + 1)M_1^2} \quad (5.4)$$

$$\frac{p_{02}}{p_{01}} = \left(\frac{T_2}{T_1} \right)^{\frac{\gamma}{\gamma-1}} \frac{p_1}{p_2} \quad (5.5)$$

$$\frac{T_{02}}{T_{01}} = 1 \quad (5.6)$$

The properties in front of the shock, closer to the inlet and denoted by subscript 1, were taken at the location of maximum Mach number. The post-shock values downstream, denoted by subscript 2, were defined where the Mach number was closest to the predicted value.

Table 5.1: Simulated and analytical ratios across the central normal shock.

| | M_1 | M_2 | $\frac{p_2}{p_1}$ | $\frac{T_2}{T_1}$ | $\frac{p_{02}}{p_{01}}$ | $\frac{T_{02}}{T_{01}}$ |
|------------|-------|-------|-------------------|-------------------|-------------------------|-------------------------|
| Simulation | 3.32 | 0.462 | 12.0 | 3.06 | 0.235 | 0.996 |
| Analytical | - | 0.458 | 12.7 | 3.08 | 0.248 | 1.000 |
| Error (%) | - | -0.9% | 5% | 0.5% | 5% | 0.4% |

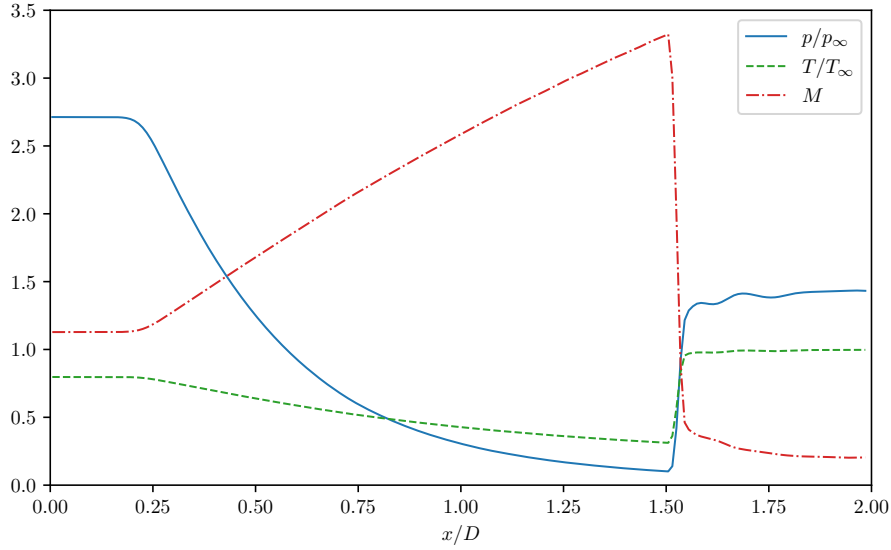


Figure 5.4: Static temperature, pressure and Mach number along centre-line. Normalized by free-stream values.

5.2 Turbulent Hydrogen Mixing Jet

The ability to model turbulent mixing was assessed by recreating the experiment of Eggers [35] where a subsonic jet of pure hydrogen was injected into a supersonic free-stream. Measurements by Eggers indicate

speeds of Mach 1.32 and 0.88 for the free-stream and hydrogen jet, respectively, which were kept at low temperatures to effectively eliminate the presence of chemical reactions. Hydrogen composition and velocity data were recorded at various stream-wise locations across the jet diameter. And while hydrogen composition was directly measured, velocity was not, it was calculated from total pressure measurements assuming a constant static pressure throughout the domain. In light of this, velocity profiles were converted back into total pressure profiles for the analysis below. To validate their data, Eggers [35] calculated the total mass flow rate at each stream-wise section, finding that integrated measurements under-predicted mass flow by 3% on average, which this report assumes to be the experimental error.

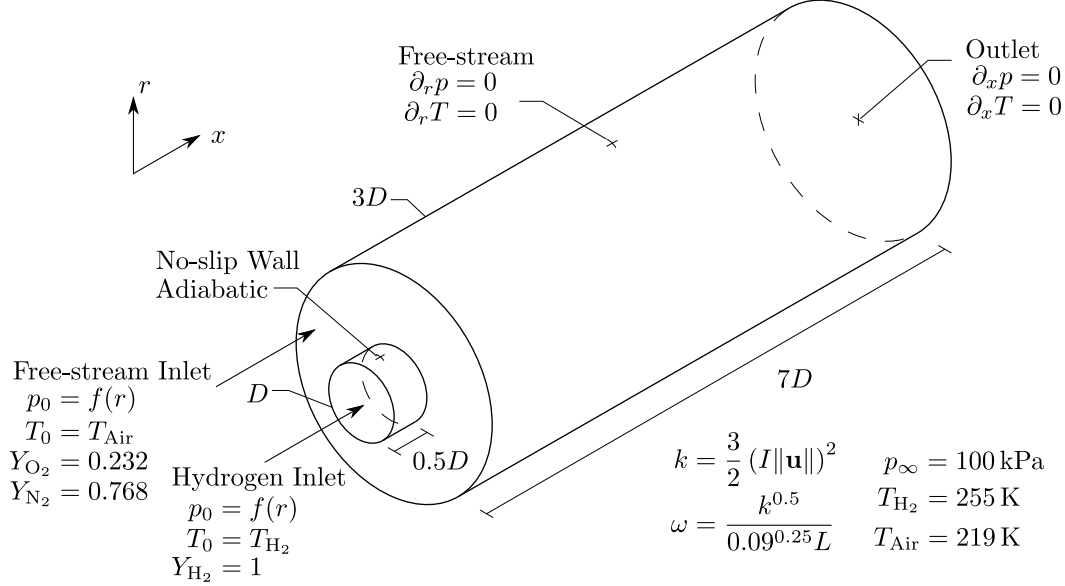


Figure 5.5: Computational domain and boundary conditions for turbulent mixing study.

Though present in the physical experiment, the computational domain used by this report, depicted in figure 5.5, neglects to model the lip thickness of the injector as it was several orders of magnitude smaller than the jet diameter. Total pressure profiles for the inlets were determined by interpolating results from the experimental data, frozen chemistry and $\text{Pr}_t = \text{Sc}_t = 0.7$ were assumed. The two equation $k - \omega$ SST model was used for turbulence modelling, where inlet profiles for k and ω , turbulent kinetic energy and dissipation rate, were estimated by isotropic relations [36]:

$$k = \frac{3}{2} (I \|\mathbf{u}\|)^2 \quad (5.7)$$

$$\omega = \frac{k^{0.5}}{0.09^{0.25} L} \quad (5.8)$$

Turbulent intensity, I , and integral length, L , were determined from the empirical relations for fully developed pipe and wall bounded flows [36], calculated to be $I = 2.7\%$, $L_{\text{H}_2} = 0.8 \text{ mm}$ and $L_\infty = 3.2 \text{ mm}$.

Grid convergence is demonstrated in figure 5.6 comparing coarse, medium, and fine meshes with 5165, 8721 and 12530 cells, which can also be characterized by 50, 75 and 100 cells spanning across the hydrogen inlet, respectively. Steady state convergence is also demonstrated in appendix B. Immediately apparent is the bifurcation in the experimental profiles, this is because, rather than precisely aligning probes with the centre-line, Eggers [35] took measurements across the entire diameter and set the point $r = 0$ to the maximum hydrogen mass fraction. However, this begs the question of why such asymmetry, particularly with the total pressure, was observed, unfortunately Eggers [35] does not address this. Given how closely the results in figure 5.6 follow one side of the bifurcated pressure distribution, the bifurcation is likely a measurement caused outlier and does not represent physical asymmetry.

The effect of turbulent inlet conditions was studied, testing different combinations of turbulent intensity and integral length. Two methods of estimating turbulent length were considered, the empirical relations [36]

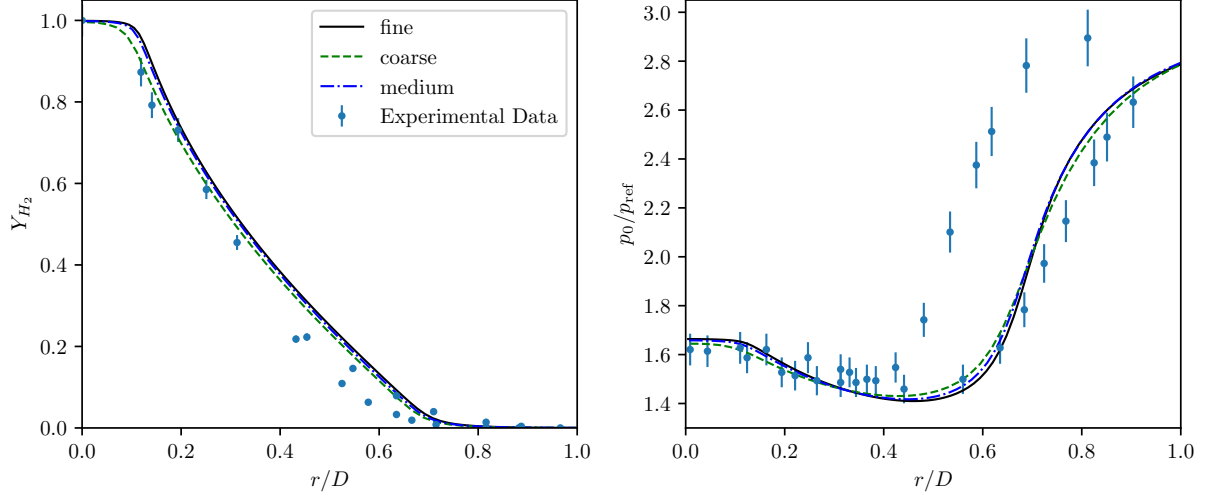


Figure 5.6: Hydrogen (left) and total pressure (right) radial profiles at stream-wise location $x/D = 5.51$ for different mesh sizes. Comparing coarse (5156 cells), medium (8721 cells) and fine (12530 cells).

Table 5.2: Turbulent integral lengths computed with different methods.

| | L_{H_2} | L_∞ |
|--------------------------------|-----------|------------|
| Method 1 - Limiting case | 11.6 mm | 8.1 mm |
| Method 2 - Empirical relations | 0.8 mm | 3.2 mm |

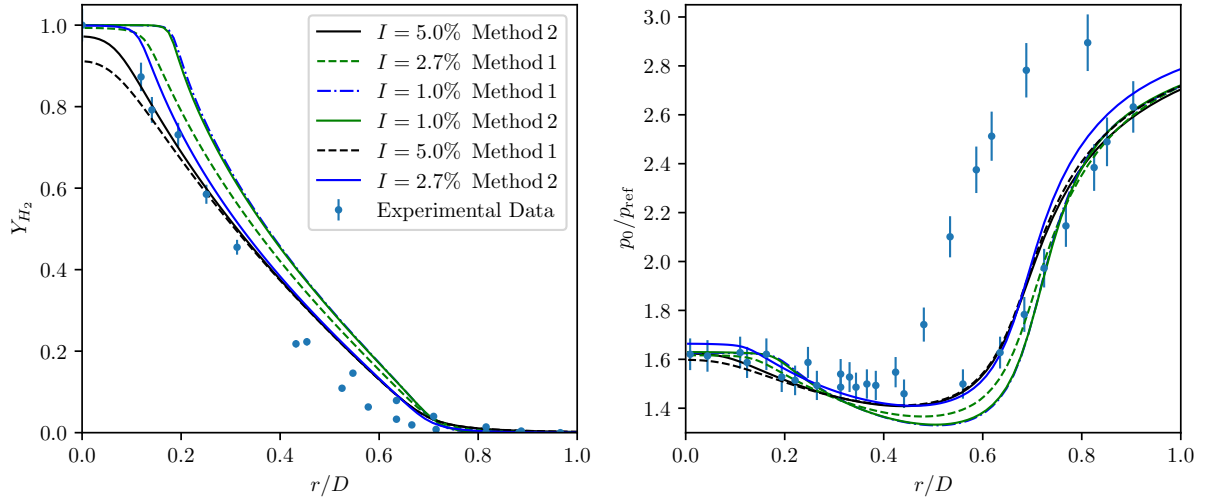


Figure 5.7: Hydrogen (left) and total pressure (right) radial profiles at stream-wise location $x/D = 5.51$ for different inlet turbulence profiles.

referred to previously and another based around physical arguments. For pipe flow, turbulent eddies cannot be larger than the diameter, and for boundary layer flows, such as the free-stream inlet, the limit is dictated by the instantaneous boundary layer thickness. Given low turbulent fluctuations, like those seen in the free-stream, a reasonable assumption is that instantaneous and time averaged boundary layer thicknesses share similar scales and was estimated from experimental data. The resulting lengths for both of these methods

are summarized in table 5.2 and turbulent intensity was also varied between 1% and 5%, the results of which are shown in figure 5.7.

For both estimation methods, the profiles with $I = 1\%$ and 2.7% predict a solid, untouched hydrogen core at the stream-wise location $x/D = 5.51$, something that was not observed in the experimental data. Also apparent is that profiles of the same turbulent intensity are in proximity to each other, indicating that turbulence is more sensitive to variation in inlet intensity than integral length. Nevertheless, the same general trend is observed in all the data and, except for $I = 1\%$, are close to the experimental values.

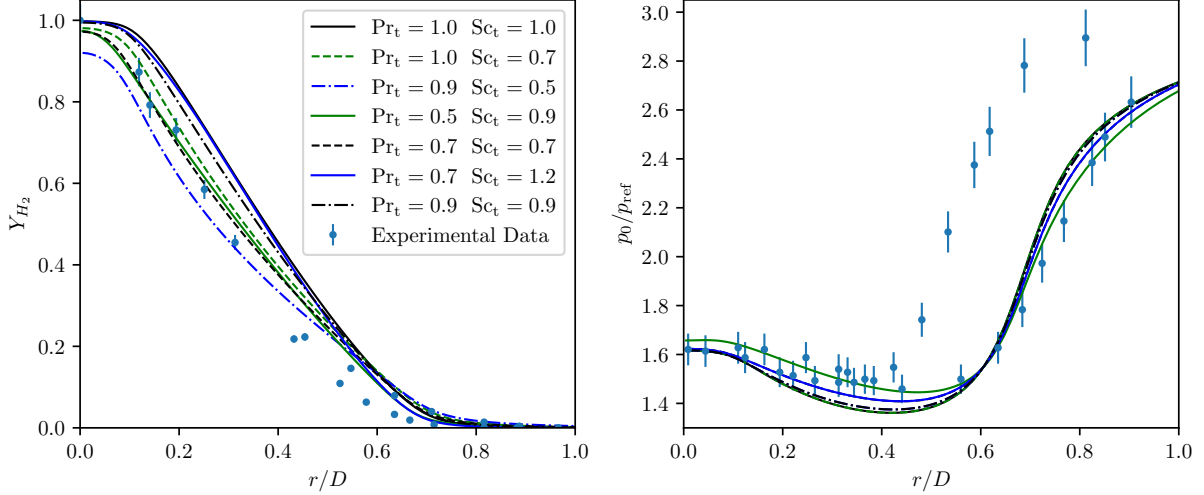


Figure 5.8: Hydrogen (left) and total pressure (right) radial profiles at stream-wise location $x/D = 5.51$ for different Pr_t/Sc_t pairs.

Sensitivity studies were also run for turbulent Prandtl and Schmidt numbers, varying them between 0.5 to 1.2, and are shown in figure 5.8. This Pr_t/Sc_t study used $I = 5\%$ and the integral lengths from method 2 as these were the closest fitting curves in figure 5.7. Like all others, the radial profiles in figure 5.8 all display the same behaviour. While these combinations cause a great deal of deviation in hydrogen mass fraction profiles, the values Pr_t/Sc_t have less of an effect on the total pressure profiles. This was somewhat to be expected, as the momentum equation can be decoupled from the energy and mass fraction equations under reasonable assumptions. Further examination of figure 5.8 reveals that the best fitting profiles had values of Pr_t and Sc_t slightly less than unity, ranging from 0.7 to 0.9.

5.3 Hydrogen-Oxygen Channel Combustion

The validation case of Mani et al. [37], with numerical data given by DalBello and Vyas [38], is a laminar one-dimensional combustion channel where molecular hydrogen and oxygen are the reacting fluids. In their numerical simulations, Mani et al. [37] obtained a closed form solution assuming six species and eight reactions, identical to the mechanism in table 5.3 without nitrogen, solved using a Runge-Kutta scheme. A mixture of molecular hydrogen and oxygen flows into the combustion chamber at Mach 1.82 and 1389 K, with the full boundary conditions given in figure 5.9.

The seven species, eight reaction mechanism of Evens and Schexnayder [39], shown in table 5.3, was used for this validation study. Grid convergence is confirmed in figure 5.10 comparing stream-wise oxygen mass fraction profiles assessed using 400, 600 and 800 cells, coarse, medium and fine sizes respectively. Figure 5.11 compares the resulting stream-wise mass fraction profiles obtained using OpenFOAM and the fine mesh to the numerical results of Mani et al. [37], revealing a good level of agreement between the two calculation methods.

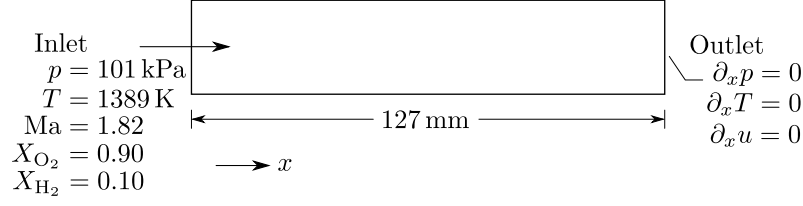


Figure 5.9: Computational domain and boundary conditions for channel combustion.

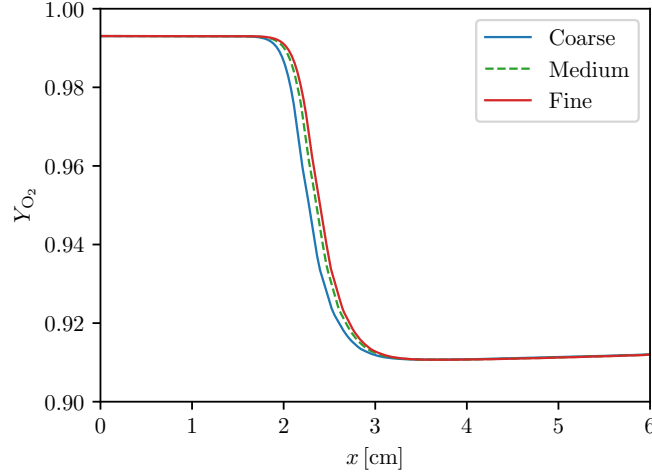


Figure 5.10: Stream-wise oxygen mass fraction profiles for different mesh sizes. One dimensional mesh with 400 (coarse), 600 (medium) and 800 (fine) cells in the stream-wise direction.

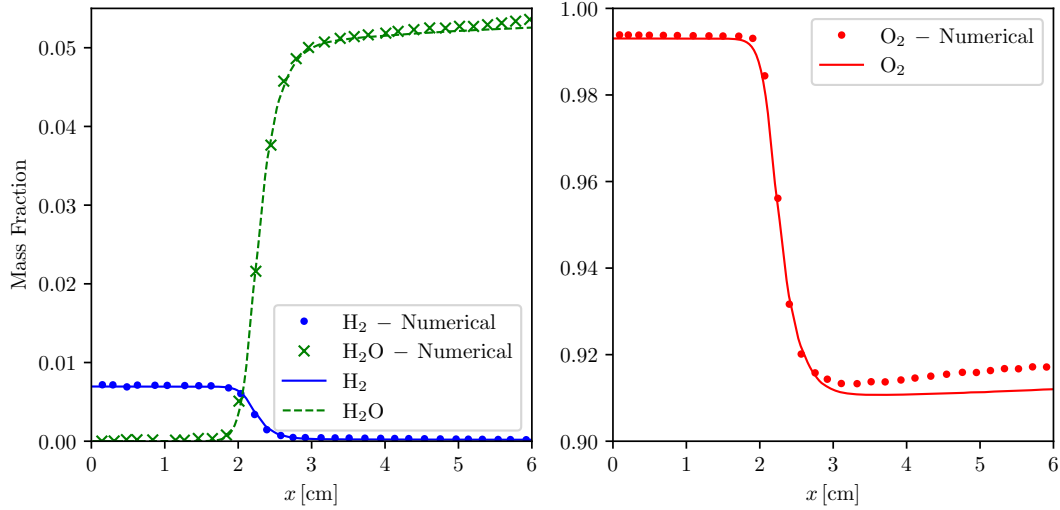


Figure 5.11: Stream-wise mass fraction profiles compared to the numerical experiment of Mani et al. [38].

5.4 Hydrocarbon Abstraction Mechanism

The two main fuels that have been studied for use in scramjets are hydrogen, requiring cryogenic storage but offering the highest performance, and kerosene, easier to store and already use in aviation fuel. Specifically,

Table 5.3: Seven species, eight reaction mechanism of Evans and Schexnayder [39].

| Species | | Reactions | |
|------------------|----------------|--|---|
| H | O ₂ | H ₂ + M \rightleftharpoons 2H + M | H ₂ O + O \rightleftharpoons 2OH |
| O | H ₂ | O ₂ + M \rightleftharpoons 2O + M | H ₂ O + H \rightleftharpoons OH + H ₂ |
| H ₂ O | N ₂ | H ₂ O + M \rightleftharpoons H + OH + M | O ₂ + H \rightleftharpoons OH + O |
| OH | | OH + M \rightleftharpoons H + O + M | H ₂ + O \rightleftharpoons OH + O |

kerosene is modelled in this report by the popular Jet-A aviation fuel, chosen as it is a widely used industry standard and data availability. Unlike H₂-O₂ combustion which is relatively easy to model, see the previous section, the Jet-A reaction mechanism consists of over 300 species [40] so simplifications must be made to not add too much computational complexity. One option is to use a highly simplified global mechanism such as the one, two and five reaction models featured in Lee et al. [40], however their applicability to situations outside the experimental conditions in which they were developed is questionable. Surrogate fuels offer an alternative, one that can also be used in physical experiments, which are precise mixtures of known components with the same properties as the complex fuel being studied. Liu et al. [41] list some surrogates that have been used to model kerosene in the past, one of which is pure *n*-decane (C₁₀H₂₂) with 39 species and 207 reactions, and propose a simpler 36 species 62 reaction model.

Table 5.4: Generalized hydrocarbon mechanism from Jachimowski [42] including N₂ as inert gas.

| Species | Reactions | |
|-------------------------------|---|--|
| $\overline{\text{CH}_2}$ | $\overline{\text{CH}_2} + \text{O}_2 \rightleftharpoons \overline{\text{CH}} + \text{HO}_2$ | $2\text{OH} \rightleftharpoons \text{H}_2\text{O} + \text{O}$ |
| $\overline{\text{CH}}$ | $\text{H} + \overline{\text{CH}_2} \rightleftharpoons \overline{\text{CH}} + \text{H}_2$ | $\text{H} + \text{OH} + \text{M} \rightleftharpoons \text{H}_2\text{O} + \text{M}$ |
| $\overline{\text{C}}$ | $\text{O} + \overline{\text{CH}_2} \rightleftharpoons \overline{\text{CH}} + \text{OH}$ | $2\text{H} + \text{M} \rightleftharpoons \text{H}_2 + \text{M}$ |
| O | $\text{OH} + \overline{\text{CH}_2} \rightleftharpoons \overline{\text{CH}} + \text{H}_2\text{O}$ | $\text{H} + \text{O}_2 + \text{M} \rightleftharpoons \text{HO}_2 + \text{M}$ |
| O ₂ | $\overline{\text{CH}} + \text{O}_2 \rightleftharpoons \overline{\text{C}} + \text{HO}_2$ | $\text{HO}_2 + \text{OH} \rightleftharpoons \text{H}_2\text{O} + \text{O}_2$ |
| H | $\text{HO}_2 + \overline{\text{CH}_2} \rightleftharpoons \overline{\text{CH}} + \text{H}_2\text{O}_2$ | $\text{HO}_2 + \text{H} \rightleftharpoons \text{H}_2 + \text{O}_2$ |
| H ₂ | $\overline{\text{CH}} \rightleftharpoons \overline{\text{C}} + \text{H}$ | $\text{HO}_2 + \text{H} \rightleftharpoons 2\text{OH}$ |
| OH | $\overline{\text{C}} + \text{OH} \rightleftharpoons \text{CO} + \text{H}$ | $\text{HO}_2 + \text{O} \rightleftharpoons \text{OH} + \text{O}_2$ |
| H ₂ O | $\text{CO} + \text{OH} \rightleftharpoons \text{CO}_2 + \text{H}$ | $2\text{HO}_2 \rightleftharpoons \text{H}_2\text{O}_2 + \text{O}_2$ |
| HO ₂ | $\text{CO} + \text{O} + \text{M} \rightleftharpoons \text{CO}_2 + \text{M}$ | $\text{HO}_2 + \text{H}_2 \rightleftharpoons \text{H}_2\text{O}_2 + \text{H}$ |
| H ₂ O ₂ | $\text{HO}_2 + \text{CO} \rightleftharpoons \text{OH} + \text{CO}_2$ | $\text{H}_2\text{O}_2 + \text{OH} \rightleftharpoons \text{HO}_2 + \text{H}_2\text{O}$ |
| CO | $\text{H} + \text{O}_2 \rightleftharpoons \text{OH} + \text{O}$ | $\text{M} + \text{H}_2\text{O}_2 \rightleftharpoons 2\text{OH} + \text{M}$ |
| CO ₂ | $\text{OH} + \text{H}_2 \rightleftharpoons \text{H}_2\text{O} + \text{H}$ | |
| N ₂ | $\text{O} + \text{H}_2 \rightleftharpoons \text{H} + \text{OH}$ | |

In light of the need to keep the already highly complex CFD simulation as simple as possible while still being applicable to a wide range of conditions, the generalized hydrocarbon mechanism by Jachimowski [42] was used to model Jet-A aviation fuel. This 13 species 26 reaction mechanism, shown in table 5.4, works by generalizing hydrocarbons from C_nH_{2n} to $\overline{\text{CH}_2}$ radicals, which decompose into the abstracted molecules $\overline{\text{CH}}$ and $\overline{\text{C}}$, equating the reaction rates to their equivalent propane/air reactions, another mechanism extensively studied by Jachimowski [43]. The specific, per mass, thermodynamic quantities for $\overline{\text{CH}_2}$ and Jet-A are set equal, with quantities for $\overline{\text{CH}}$ and $\overline{\text{C}}$ determined by setting the heat of reaction to their propane equivalents [44], that is:

$$h(\overline{\text{CH}}) = h(\overline{\text{CH}_2}) + h(\text{C}_3\text{H}_7) - h(\text{C}_3\text{H}_8) \quad (5.9)$$

$$h(\overline{\text{C}}) = h(\overline{\text{CH}}) + h(\text{C}_3\text{H}_6) - h(\text{C}_3\text{H}_7) \quad (5.10)$$

$$s(\overline{\text{CH}}) = s(\overline{\text{CH}_2}) + s(\text{C}_3\text{H}_7) - s(\text{C}_3\text{H}_8) \quad (5.11)$$

$$s(\overline{\text{C}}) = s(\overline{\text{CH}}) + s(\text{C}_3\text{H}_6) - s(\text{C}_3\text{H}_7) \quad (5.12)$$

and used to determine the equilibrium constants. Additional physical quantities for Jet-A, molecular viscosity and thermal conductivity, were taken from the experimental relations by Rachner [45]. The calculation methods are elaborated on in appendix A along with the Jet-A parameters used in this report.

To verify this mechanism for Jet-A, ignition delay times were computed using OpenFOAM and Cantera, an open-source set of chemistry tools used to obtain data over a wide range of conditions, and compared to experimental data from Vasu et al. [46] in figure 5.12. Included in this comparison is data for *n*-dodecane, $C_{12}H_{26}$ another jet fuel surrogate, simulated with Cantera using the 100 species 432 reaction mechanism developed by Wang et al. [47]. Ignition delay times for *n*-dodecane were included to demonstrate the difficulty of precisely modelling complex hydrocarbons and that the error between experiment and the generalized hydrocarbon mechanism, while large, are not outside the realm of acceptability even for a 432 step mechanism. To get a sense of the errors this will cause in CFD simulations, the error in ignition delay time is on the order of 50 μs and taking a representative hypersonic velocity of 1000 m/s equates to linear errors on the order of 50 mm, small when compared to a 1 m long engine.

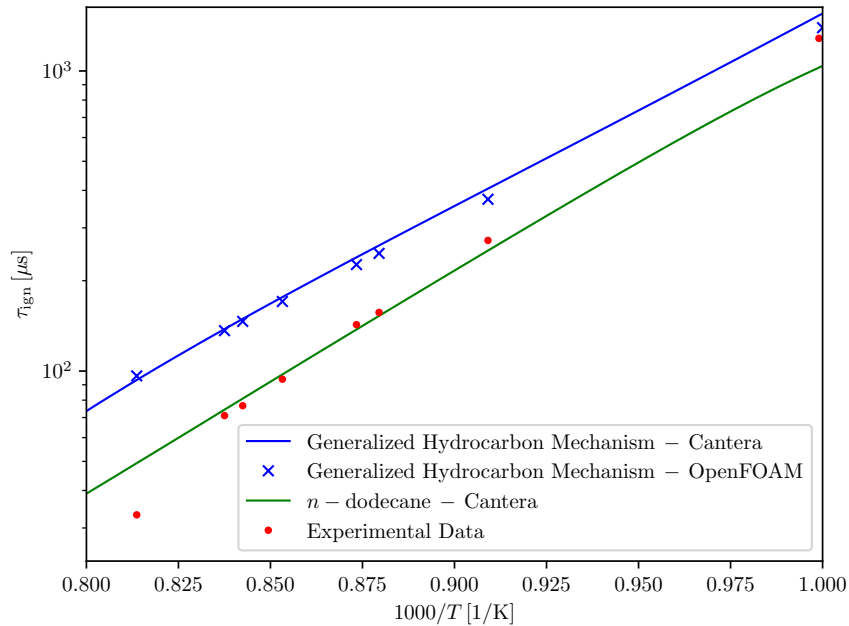


Figure 5.12: Ignition delay times for Jet-A in air, $p = 20$ atm and $\Phi = 1.0$, computed using the generalized hydrocarbon mechanism of Jachimowski [42]. Ignition times for *n*-dodecane computed using the mechanism of Wang et al. [47]. Experimental data from Vasu et al. [46].

Chapter 6

Experiment of Yang et al. [6]

In the experiment of Yang et al. [6], a scramjet was simulated, both numerically and experimentally, using kerosene fuel injected via a central strut and a pair of transverse high temperature jets (THTJ) downstream to induce instabilities. The computational domain, shown in figure 6.1, consists of a constant area isolator and a combustor made up of divergent and constant area sections. Dimensions, where unlisted by Yang et al. [6], were assumed based off of the figures provided. Boundary conditions for the inlet, THTJ and injector, where mass flow rate is fixed using an equivalence ratio of 0.8, are given in table 6.1, and zero stream-wise gradient conditions were prescribed at the outlet. Turbulence was modelled using $k - \omega$ SST and turbulent inlet conditions were generated using the isotropic relations given in equations (5.7) and (5.8), assuming 3% turbulent intensity. Integral lengths were 3 mm for the inlet, using the empirical relations for wall bounded flows [36], and 0.8 mm for the injector and THTJ, using the jet diameter.

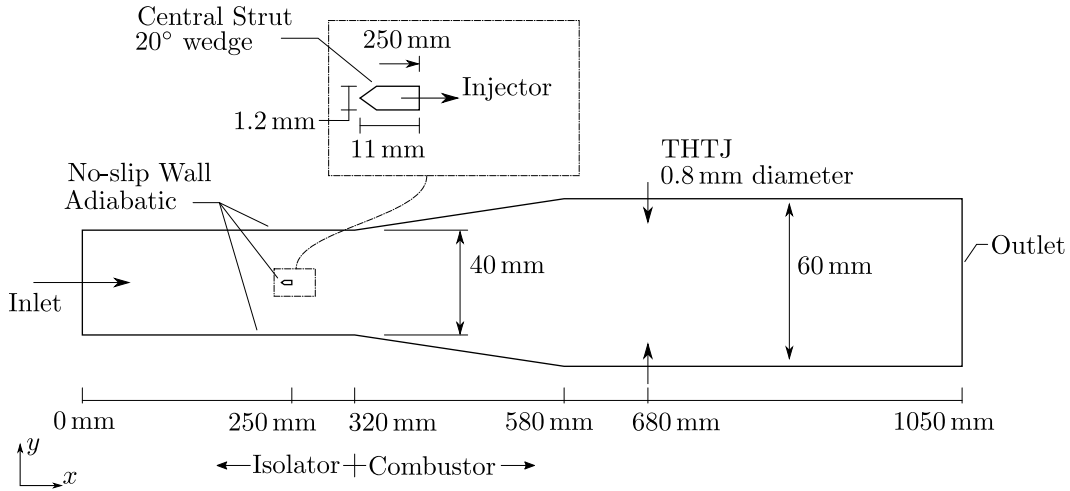


Figure 6.1: Computational domain for recreation of Yang et al. experiment. Not to scale.

Table 6.1: Boundary conditions used to recreate the experiment of Yang et al. [6].

| | | | | | |
|----------|---------------------------------|----------------------------------|---------------------------|---------------------------------|---------------------------|
| Inlet | $p_0 = 1970 \text{ kPa}$ | $T_0 = 1520 \text{ K}$ | $\text{Ma} = 2.52$ | $Y_{\text{N}_2} = 0.77$ | $Y_{\text{O}_2} = 0.23$ |
| THTJ | $p_0 = 3350 \text{ kPa}$ | $T_0 = 2700 \text{ K}$ | $\text{Ma} = 1.47$ | $Y_{\text{CO}} = 0.44$ | $Y_{\text{CO}_2} = 0.23$ |
| | | | | $Y_{\text{H}_2\text{O}} = 0.23$ | $Y_{\text{Jet-A}} = 0.10$ |
| Injector | $\partial_x p = 0$ ¹ | $T = 300 \text{ K}$ ¹ | $\Phi = 0.8$ ² | $Y_{\text{Jet-A}} = 1.00$ | |

¹ Assumption.

² Equivalence ratio used to define mass flow rate.

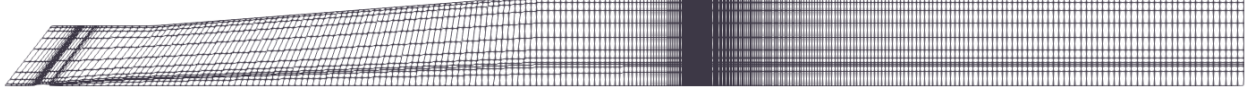


Figure 6.2: Coarse mesh used for the recreation of Yang et al. experiment. Showing every second grid line.

The mesh was a block structured mesh shown in figure 6.2, chosen because of the difficulty experienced capturing shocks with unstructured meshes in hy2Foam. For the frozen chemistry cases, the first 220 mm of the isolator was simulated separately to provide inflow conditions and reduce mesh size, justified since the flow is supersonic. The mesh was skewed at 33° from the centre-line for the rest of the isolator in anticipation of the oblique shock wave formed by the strut. Centre-line symmetry was assumed except in the reacting flow case, as Yang et al. observed asymmetry in these simulations. Wall pressures for coarse, medium, and fine mesh sizes, 17 516, 67 690 and 154 747 cells respectively, are shown in figure 6.3, demonstrating convergence. With this demonstrated, the medium-sized mesh will be used for analysis. Steady state convergence was also demonstrated in appendix B.

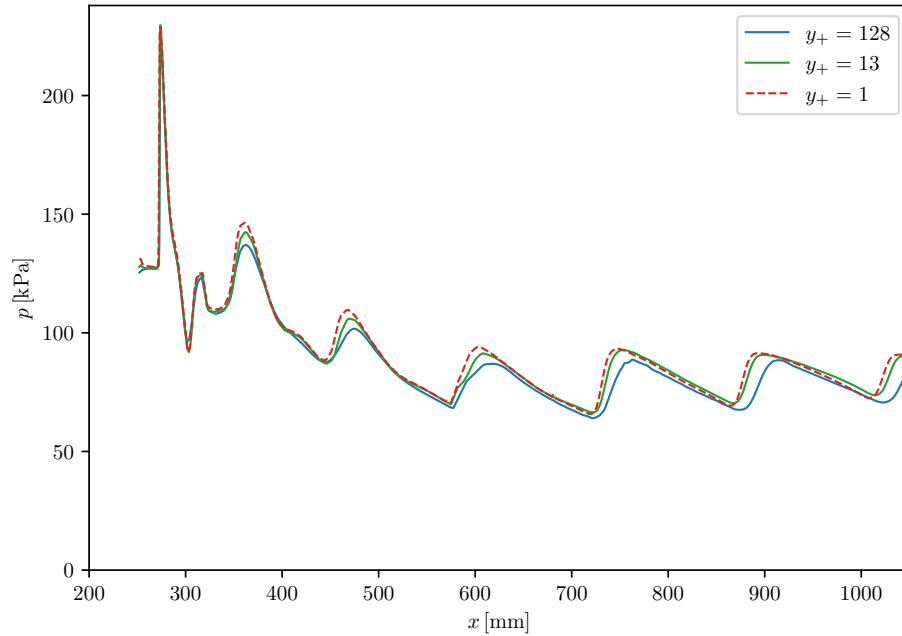


Figure 6.3: Wall static pressure for different mesh sizes. y_+ values are 128, coarse, 13, medium, and 1, fine. Frozen case with only strut injector enabled.

Results for the frozen cases, both with and without the THTJ, are presented in figures 6.5, 6.6, and 6.7, fuel mass fraction, pressure, and artificial Schlieren respectively, which show similar structures to those obtained by Yang et al. [6]. Not much is to be said for the case with only the strut injector enabled since it is essentially just a free turbulent jet. Shock structures still appear in this case and can be seen in figure 6.7, though these are relatively weak and have little effect on the flow. Introduction of the THTJ results in a much stronger shock train, seen in figure 6.6 as well as 6.7, and resemble bow shocks near the walls, indeed they start off this way. A far more complex structure can be seen upstream of the THTJ, one that is not easily categorized, displaying an almost circular symmetry and does not occur if the no-slip condition is neglected, suggesting it is a viscous phenomenon. Inspecting the streamline plot in figure 6.8 reveals that this behaviour is caused by a recirculation zone acting as a converging diverging nozzle, one that produces its own weaker shock train interlaced with the one caused by the THTJ.

One definition of mixing efficiency, as defined by Yang et al. [6], is:

$$\eta_m = \frac{\dot{m}_{f,\text{mixed}}}{\dot{m}_f} = \frac{\int Y_{\text{react}} \rho u_x dA}{\int Y_f \rho u_x dA} \quad (6.1)$$

$$Y_{\text{react}} = \begin{cases} Y_f & \text{for } Y_f \leq Y_{\text{stoic}} \\ \frac{Y_{\text{stoic}}(1 - Y_f)}{1 - Y_{\text{stoic}}} & \text{else} \end{cases} \quad (6.2)$$

where u_x is the stream-wise velocity, A is the cross-sectional area, subscript f denotes the fuel and Y_{stoic} is the fuel mass fraction in a stoichiometric fuel-air mixture. The variable Y_{react} measures the fraction of fuel that would react given infinitely fast chemistry and making the simplifying assumption that the only species are fuel and air. Mixing efficiencies for cases with and without the THTJ are shown in figure 6.4 and demonstrate the effectiveness of increasing mixing through the THTJ. Results presented here show a much larger growth in mixing efficiency with the THTJ than what is obtained by Yang et al. [6], the cause of this is also thought to be caused by the recirculation zones.

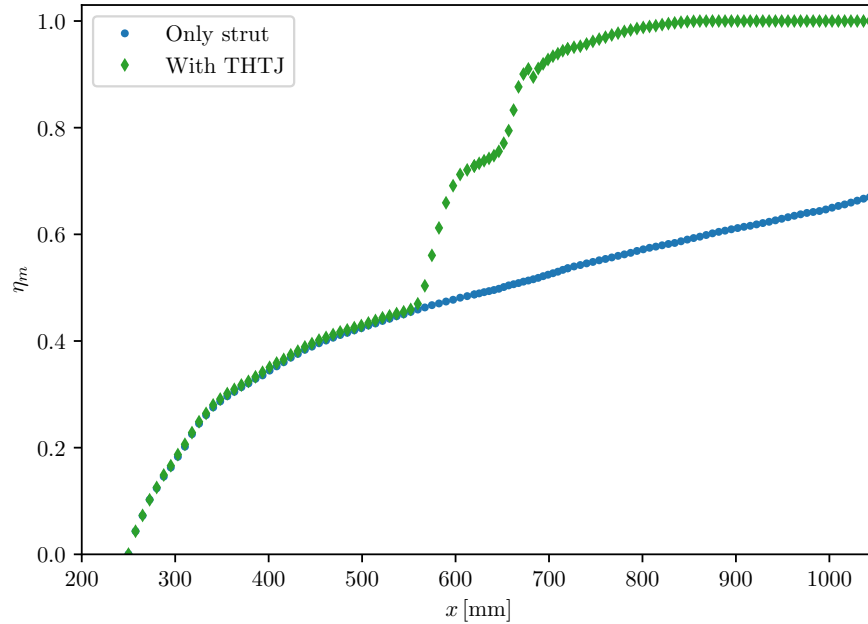


Figure 6.4: Mixing efficiencies for engine with only the strut injector enabled and with THTJ. Using frozen chemistry.

Results from the reacting case are shown in figures 6.9 and 6.10 showing an engine that is mostly subsonic, in stark contrast to the fully supersonic results obtained by Yang et al. [6]. The reacting case abandoned the assumption of centre-line symmetry, did not use a separate inlet simulation and extended the inlet and outlet into the free-stream. As stated previously, Jet-A fuel was modelled using the generalized hydrocarbon mechanism of Jachimowski [42]. This subsonic result appears to be converged, as variations in inlet and outlet boundary conditions produce similar results. The presence of recirculation zones, which do not appear to be seen by Yang et al. [6], and higher pressures in the frozen case seem to suggest that this disagreement is a result of the flow properties. However, the engine also becomes subsonic when only the strut injector was enabled, and increased in temperature to maintain combustion as discussed below, suggesting the error lies with reacting model.

While the attempt to recreate the scramjet of Yang et al. has been unsuccessful, particularly in the reacting case, that is not to say that observations were not made. During testing, it was found that the engine would not ignite without THTJ, further supported by additional one-dimensional testing. Referring back to figure 5.12, the reason becomes clear as ignition delay times for Jet-A at temperatures ≤ 1000 K are

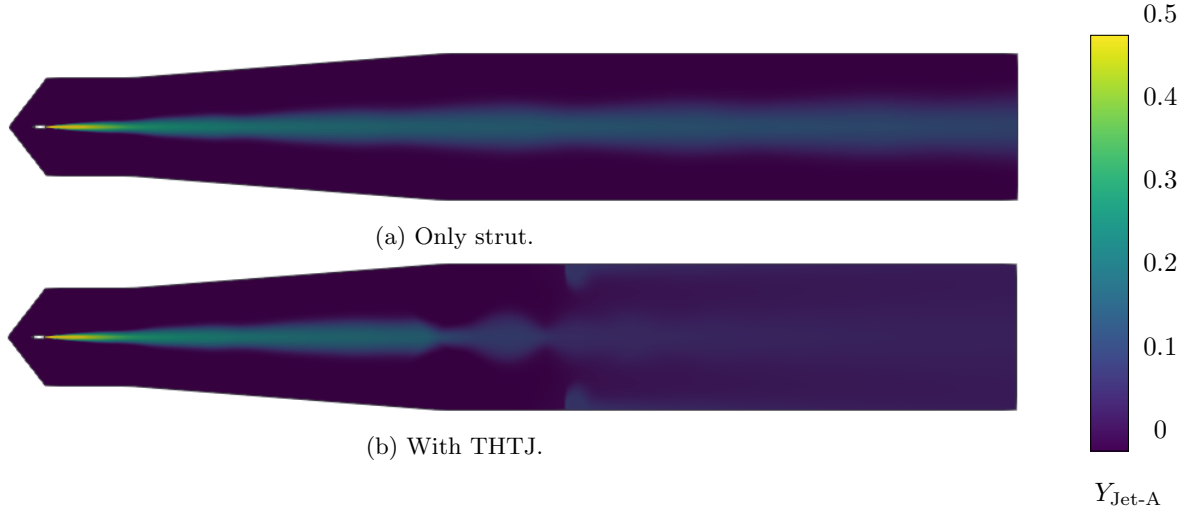


Figure 6.5: Jet-A mass fraction distribution for frozen chemistry cases. Not to scale.

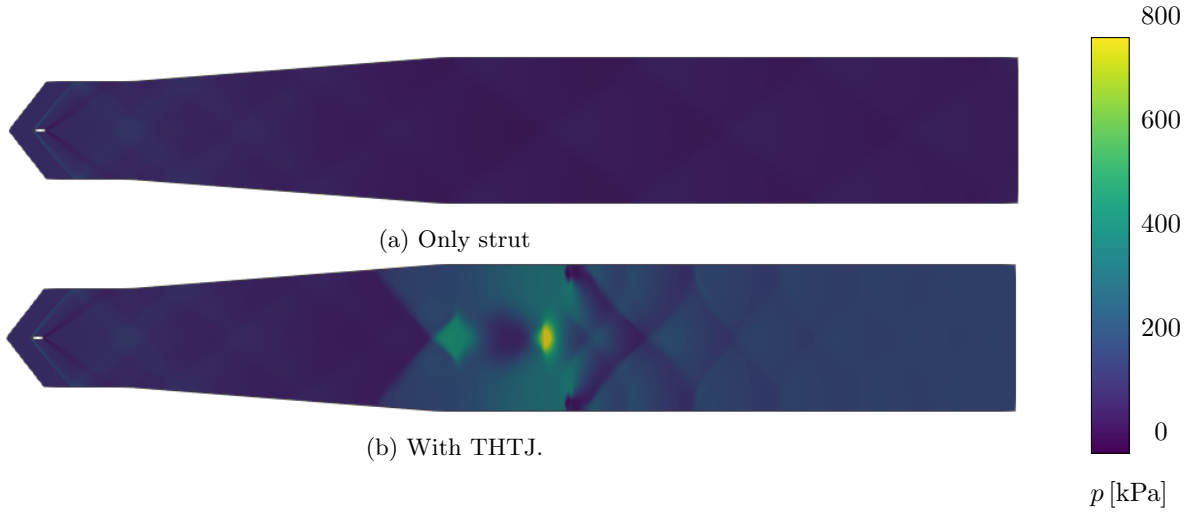


Figure 6.6: Static pressure distribution for frozen chemistry cases. Not to scale.

on the order of 1 ms. Taking a representative velocity of 1000 m/s, this suggests an ignition point 1 m away from the central strut which means the fuel will ignite close to, if not past, the outlet. It was found that temperatures close to 1500 K, the stagnation temperature of the inflow, were needed for the flame to ignite without the THTJ. From this we can conclude that the presence of THTJ is not just to induce the RMI and promote mixing, but is a necessary part of ignition.

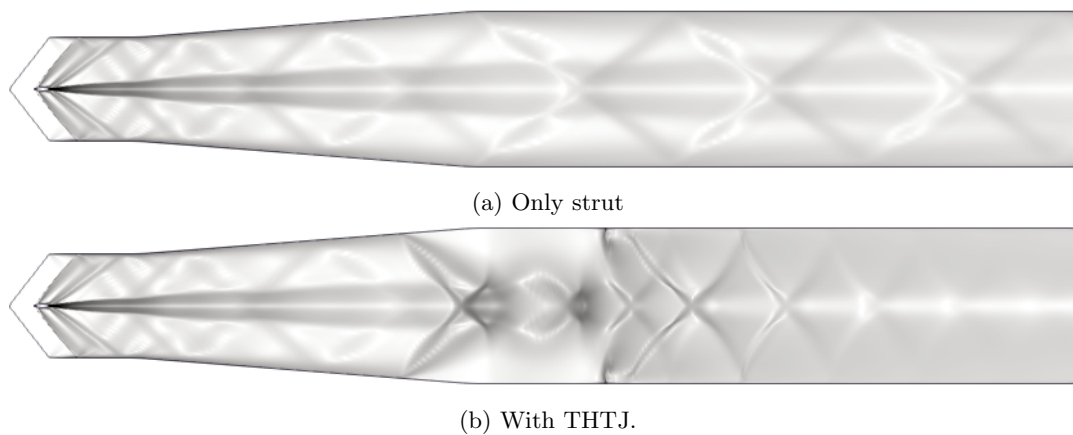


Figure 6.7: Artificial Schlieren images showing shock structure. Using a logarithmic mapping. Not to scale.

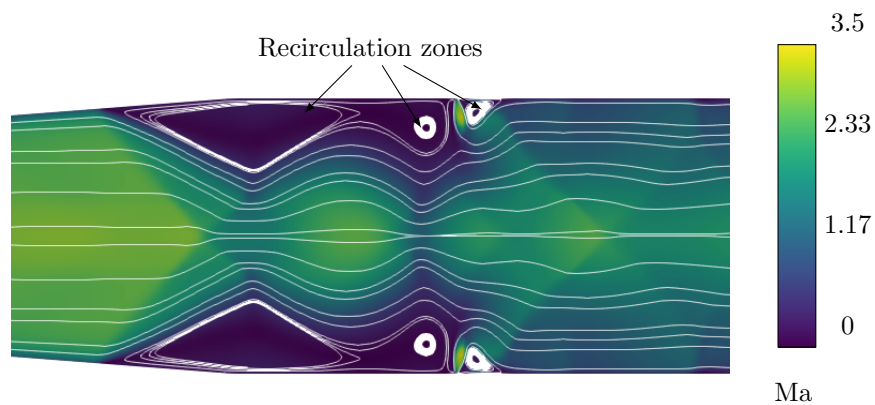


Figure 6.8: Streamlines and Mach number in combustor section showing recirculation zones. Frozen case with THTJ. Not to scale.

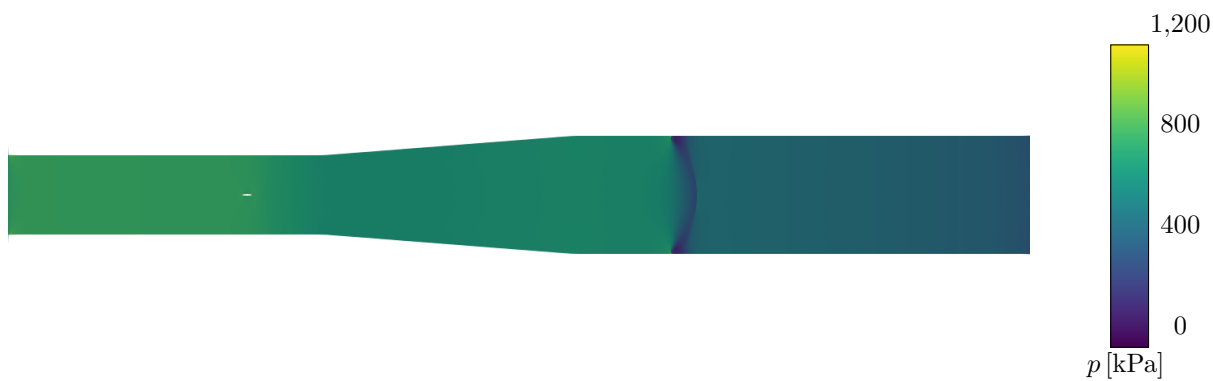


Figure 6.9: Pressure distribution in reacting case. Not to scale.

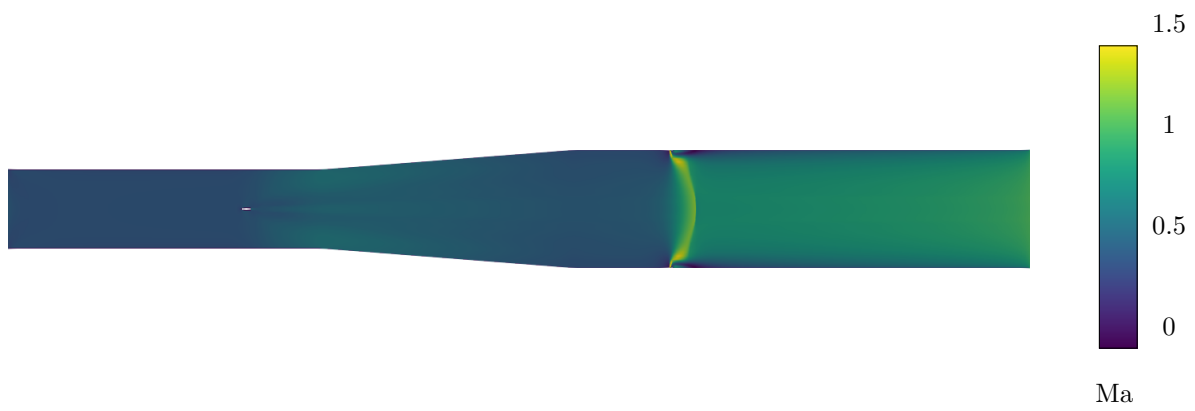


Figure 6.10: Mach number distribution in reacting case. Not to scale.

Chapter 7

Conclusion and Recommendations for Future Work

In order for the dream of widespread space travel to become a reality, orbital launch vehicles need to be made cheap, reliable and robust. One way to achieve this is by using air-breathing engines utilizing oxygen in the atmosphere unlike rockets, making air-breathing propulsion much more efficient. Scramjets, which operate at hypersonic speeds, pose interesting challenges for combustor design: how to properly mix fuel and air when residence times are measured in milliseconds. This question has been an area of much research and mixing enhancement techniques include lobed splitter plates, wall mounted ramps and struts with the aim of increasing turbulence [7]. Another method is to use the properties of shock to induce instabilities in the mixing layer, investigated in this report. The scramjet design of Yang et al. [6] enhances mixing by using THTJ to induce RMI and reproducing this numerically was the goal of this report. This attempt was unfortunately unsuccessful as flow within the engine would become subsonic, behaviour that was not seen in either numerical or physical experiments of the original paper. However, results were still obtained for the cases with frozen chemistry, successfully demonstrating shock induced mixing enhancement via RMI. Tests in this report also found that the presence of THTJ is not just to induce instabilities, but is necessary for ignition to occur.

The popular open-source CFD software OpenFOAM was used in this report using the third party solver hy2Foam, part of the hyStrath project. Hy2Foam was selected as it uses the central schemes of Kurganov and Tadmor, shown to capture shocks better than pressure based algorithms, and its reputation, created in part by the University of Strathclyde. Modifications needed to be made, however, to include turbulent mixing terms into the governing equations validated by recreating the turbulent mixing experiment of Eggers. Other validation cases were an under-expanded jet, evaluating the ability of hy2Foam to capture shock structures, and a one-dimensional reacting channel to demonstrate combustion modelling. In lieu of a more complicated reaction mechanism, kerosene fuel, specifically Jet-A, was modelled using the generalized hydrocarbon mechanism of Jachimowski et al. [42]. This simplified mechanism was evaluated against experimental Jet-A ignition delay times [46] where large relative errors were seen. The generalized hydrocarbon mechanism was still used because the difference in delay times would correspond to linear errors less than 5% of the engine length at supersonic speeds.

This report was unable to recreate the reacting case of Yang et al. [6] and any continuation of this project would have to rectify this. After these issues are resolved, however, the next step would be to improve upon or optimize this design. Here, optimization refers to changing the parameters, dimensions, THTJ angle, etc., and not adding new structures or drastically changing the flow which would be under the purview of improvement. Optimization of the Yang et al. [6] design would still be beneficial because its simplicity would make it an ideal testbed for multi-variable optimization techniques [48] even if improvements yield a better performing engine. Mixing could be further improved by introducing additional struts or wall mounted ramps to the flow. Another consideration is if mixing and ignition steps should be separated as this report found that the THTJ is necessary for ignition. With these steps separated, other modes of igniting the fuel can be considered, such as shock-induced ignition [49].

Besides optimization and improvement, turbulent sensitivity, in the form of inlet conditions and turbu-

lence models, needs to be evaluated. The first section of the Yang et al. [6] design is referred to as an isolator, this should be verified. Sensitivity studies also need to be preformed for the chemical reaction rate constants, hydrocarbon fuels are never precise mixtures and an engine using them needs to be robust in this regard. Hy2Foam should receive additional verification and validation for turbulent reacting flows, if for no other reason than to eliminate the solver as a source of error in this report. For these purposes it is recommended by the author to use hydrogen combustors as the reaction mechanism is simpler and will largely eliminate doubt in this area. Modifications to hy2Foam, besides those made in this report, are needed to fully utilize the turbulent models available in OpenFOAM and will surely benefit future researchers.

Bibliography

- [1] “Atlas V Launch Services User’s Guide,” United Launch Alliance, Manual, 2010. [Online]. Available: https://www.ulalaunch.com/docs/default-source/rockets/atlasvusersguide2010a.pdf?sfvrsn=f84bb59e_2
- [2] C. Segal, “PROPULSION SYSTEMS FOR HYPERSONIC FLIGHT,” in *Critical Technologies for Hypersonic Vehicle Development*. Rhode-Saint-Genese, Belgium: The von Karman Institute for Fluid Dynamics, 2004.
- [3] M. Tang and R. Chase, “The Quest for Hypersonic Flight with Air-Breathing Propulsion,” in *15th AIAA International Space Planes and Hypersonic Systems and Technologies Conference*. Dayton, Ohio: American Institute of Aeronautics and Astronautics, Apr. 2008. [Online]. Available: <https://arc.aiaa.org/doi/10.2514/6.2008-2546>
- [4] J. C. Mankins, “Highly reusable space transportation: Advanced concepts and the opening of the space frontier,” *Acta Astronautica*, vol. 51, no. 10, pp. 727–742, Nov. 2002. [Online]. Available: <https://linkinghub.elsevier.com/retrieve/pii/S0094576502000206>
- [5] K. W. Flaherty, K. M. Andrews, and G. W. Liston, “Operability Benefits of Airbreathing Hypersonic Propulsion for Flexible Access to Space,” *Journal of Spacecraft and Rockets*, vol. 47, no. 2, pp. 280–287, Mar. 2010. [Online]. Available: <https://arc.aiaa.org/doi/10.2514/1.43750>
- [6] Q. Yang, J. Chang, and W. Bao, “Richtmyer-Meshkov Instability Induced Mixing Enhancement in the Scramjet Combustor with a Central Strut,” *Advances in Mechanical Engineering*, vol. 6, p. 614189, Jan. 2014. [Online]. Available: <http://journals.sagepub.com/doi/10.1155/2014/614189>
- [7] J. Tan, D. Zhang, and L. Lv, “A review on enhanced mixing methods in supersonic mixing layer flows,” *Acta Astronautica*, vol. 152, pp. 310–324, Nov. 2018. [Online]. Available: <https://linkinghub.elsevier.com/retrieve/pii/S009457651831124X>
- [8] R. R. Shenoy, T. G. Drozda, A. T. Norris, R. A. Baurle, and J. P. Drummond, “Comparison of Mixing Characteristics for Several Fuel Injectors at Mach 8 and 15 Hypervelocity Flow Conditions,” in *2018 Joint Propulsion Conference*. Cincinnati, Ohio: American Institute of Aeronautics and Astronautics, Jul. 2018. [Online]. Available: <https://arc.aiaa.org/doi/10.2514/6.2018-4540>
- [9] B. Cheng, J. Glimm, and D. H. Sharp, “The α s and θ s in Rayleigh–Taylor and Richtmyer–Meshkov instabilities,” *Physica D: Nonlinear Phenomena*, vol. 404, p. 132356, Mar. 2020. [Online]. Available: <https://www.sciencedirect.com/science/article/pii/S0167278919302428>
- [10] M. Brouillette, “The Richtmyer-Meshkov Instability,” *Annu. Rev. Fluid Mech.*, vol. 34, no. 1, pp. 445–468, Jan. 2002. [Online]. Available: <https://www.annualreviews.org/doi/10.1146/annurev.fluid.34.090101.162238>
- [11] S. M. Flesberg, R. Taghavi, and S. Farokhi, “Mixing Enhancement in a Scramjet Combustor Using Fuel Jet Injection Swirl,” in *22nd AIAA International Space Planes and Hypersonics Systems and Technologies Conference*. Orlando, FL: American Institute of Aeronautics and Astronautics, Sep. 2018. [Online]. Available: <https://arc.aiaa.org/doi/10.2514/6.2018-5381>

- [12] F. M. White, *Viscous fluid flow*, 2nd ed., ser. McGraw-Hill series in mechanical engineering. New York: McGraw-Hill, 1991.
- [13] V. Casseau, R. Palharini, T. Scanlon, and R. Brown, “A Two-Temperature Open-Source CFD Model for Hypersonic Reacting Flows, Part One: Zero-Dimensional Analysis,” *Aerospace*, vol. 3, no. 4, p. 34, Oct. 2016. [Online]. Available: <http://www.mdpi.com/2226-4310/3/4/34>
- [14] G. V. Candler and I. Nompelis, “Computational Fluid Dynamics for Atmospheric Entry,” in *Non-Equilibrium Dynamics: From Physical Models to Hypersonic Flights*. Rhode-Saint-Genese, Belgium: The von Karman Institute for Fluid Dynamics, 2009. [Online]. Available: https://www.vki.ac.be/index.php?option=com_content&view=article&id=199&Itemid=344
- [15] S. Gordon and B. J. McBride, “Computer Program for Calculation of Complex Chemical Equilibrium Compositions and Applications I: Analysis,” NASA, NASA Reference Publication NASA-RP-1311, Oct. 1994. [Online]. Available: <https://ntrs.nasa.gov/citations/19950013764>
- [16] J. D. Anderson, *Modern compressible flow: with historical perspective*, 4th ed. New York, NY: McGraw Hill, 2021.
- [17] J. D. Anderson Jr., *Hypersonic and High-Temperature Gas Dynamics, Second Edition*. Reston, VA: American Institute of Aeronautics and Astronautics, Oct. 2006. [Online]. Available: <https://arc.aiaa.org/doi/book/10.2514/4.861956>
- [18] B. McBride and S. Gordon, “Computer Program for Calculation of Complex Chemical Equilibrium Compositions and Applications II. Users Manual and Program Description,” NASA, NASA Reference Publication NASA-RP-1311, 1996. [Online]. Available: <https://ntrs.nasa.gov/api/citations/19960044559>
- [19] J.-J. O. E. Hoste, “Scramjet Combustion Modeling Using Eddy Dissipation Model,” Ph.D. dissertation, University of Strathclyde, Glasgow, United Kingdom, 2018.
- [20] R. A. Baurle, “Modeling of High Speed Reacting Flows: Established Practices and Future Challenges,” in *42nd AIAA Aerospace Sciences Meeting and Exhibit*, Reno, NV, Jan. 2004. [Online]. Available: <https://ntrs.nasa.gov/citations/20040035566>
- [21] “Turbulence Modeling Resource.” [Online]. Available: <https://turbmodels.larc.nasa.gov/index.html>
- [22] P. A. Durbin, “Turbulence Closure Models for Computational Fluid Dynamics,” in *Encyclopedia of Computational Mechanics Second Edition*, E. Stein, R. de Borst, and T. J. R. Hughes, Eds. Chichester, UK: John Wiley & Sons, Ltd, Dec. 2017, pp. 1–22. [Online]. Available: <https://onlinelibrary.wiley.com/doi/10.1002/9781119176817.ecm2061>
- [23] “OpenFOAM | Free CFD Software | The OpenFOAM Foundation.” [Online]. Available: <https://openfoam.org/>
- [24] “OpenFOAM,” Dec. 2022. [Online]. Available: <https://www.openfoam.com/>
- [25] H. Jasak, “Error Analysis and Estimation for the Finite Volume Method with Applications to Fluid Flows,” Ph.D. dissertation, University of London, London, UK, 1996.
- [26] hyStrath, “hyStrath.” [Online]. Available: <https://hystrath.github.io/>
- [27] V. Casseau, D. Espinoza, T. Scanlon, and R. Brown, “A Two-Temperature Open-Source CFD Model for Hypersonic Reacting Flows, Part Two: Multi-Dimensional Analysis,” *Aerospace*, vol. 3, no. 4, p. 45, Dec. 2016. [Online]. Available: <http://www.mdpi.com/2226-4310/3/4/45>
- [28] C. J. Greenshields, H. G. Weller, L. Gasparini, and J. M. Reese, “Implementation of semi-discrete, non-staggered central schemes in a colocated, polyhedral, finite volume framework, for high-speed viscous flows,” *Int. J. Numer. Meth. Fluids*, pp. n/a–n/a, 2009. [Online]. Available: <https://onlinelibrary.wiley.com/doi/10.1002/fld.2069>

- [29] C. Greenshields and H. Weller, *Notes on Computational Fluid Dynamics: General Principles*. Reading, UK: CFD Direct Ltd, 2022. [Online]. Available: <https://doc.cfd.direct/notes/cfd-general-principles/>
- [30] L. F. G. Marcantoni, J. P. Tamagno, and S. A. Elaskar, “High speed flow simulation using OpenFOAM,” *Asociación Argentina de Mecánica Computacional*, p. 22, 2012.
- [31] K. W. Thompson, “Time dependent boundary conditions for hyperbolic systems,” *Journal of Computational Physics*, vol. 68, no. 1, pp. 1–24, Jan. 1987. [Online]. Available: <https://linkinghub.elsevier.com/retrieve/pii/0021999187900416>
- [32] T. J. Poinso and S. K. Lele, “Boundary Conditions for Direct Simulations of Compressible Viscous Flows,” *Journal of Computational Physics*, p. 26, 1992.
- [33] L. Selle, F. Nicoud, and T. Poinso, “Actual Impedance of Nonreflecting Boundary Conditions: Implications for Computation of Resonators,” *AIAA Journal*, vol. 42, no. 5, pp. 958–964, May 2004. [Online]. Available: <https://arc.aiaa.org/doi/10.2514/1.1883>
- [34] S. Crist, D. R. Glass, and P. M. Sherman, “Study of the highly underexpanded sonic jet.” *AIAA Journal*, vol. 4, no. 1, pp. 68–71, Jan. 1966. [Online]. Available: <https://arc.aiaa.org/doi/10.2514/3.3386>
- [35] J. M. Eggers, “Turbulent mixing of coaxial compressible hydrogen-air jets,” NASA, Tech. Rep. TN-D-6487, Sep. 1971. [Online]. Available: <https://ntrs.nasa.gov/citations/19710024807>
- [36] “Fluent User’s Guide,” ANSYS Inc., Manual, 2013.
- [37] M. Mani, R. Bush, and P. Vogel, “Implicit equilibrium and finite-rate chemistry models for high speedflow applications,” in *9th Applied Aerodynamics Conference*. Baltimore, MD, U.S.A.: American Institute of Aeronautics and Astronautics, Sep. 1991. [Online]. Available: <https://arc.aiaa.org/doi/10.2514/6.1991-3299>
- [38] T. DalBello and M. Vyas, “Channel Combustion.” [Online]. Available: <https://www.grc.nasa.gov/www/wind/valid/channel/channel.html>
- [39] J. S. Evans and C. J. Schexnayder, “Influence of Chemical Kinetics and Unmixedness on Burning in Supersonic Hydrogen Flames,” *AIAA Journal*, vol. 18, no. 2, pp. 188–193, Feb. 1980. [Online]. Available: <https://arc.aiaa.org/doi/10.2514/3.50747>
- [40] C.-M. Lee, K. Kundu, and B. Ghorashi, “Simplified jet-A kinetic mechanism for combustor application,” in *Aerospace Sciences Meeting*, Reno, NV, Jan. 1993, number: E-7457. [Online]. Available: <https://ntrs.nasa.gov/citations/19930006315>
- [41] Y. Liu, Y. Yan, C. Dai, and J. Li, “A simplified chemical reaction mechanism for surrogate fuel of aviation kerosene,” *Chem. Res. Chin. Univ.*, vol. 33, no. 2, pp. 274–281, Apr. 2017. [Online]. Available: <http://link.springer.com/10.1007/s40242-017-6280-1>
- [42] C. J. Jachimowski, “A simplified hydrocarbon reaction mechanism for combustion applications,” *Journal of Propulsion and Power*, vol. 1, no. 5, pp. 329–335, Sep. 1985. [Online]. Available: <https://arc.aiaa.org/doi/10.2514/3.22805>
- [43] —, “Chemical kinetic reaction mechanism for the combustion of propane,” *Combustion and Flame*, vol. 55, no. 2, pp. 213–224, Feb. 1984. [Online]. Available: <https://linkinghub.elsevier.com/retrieve/pii/0010218084900294>
- [44] B. J. McBride, S. Gordon, and M. A. Reno, “Coefficients for calculating thermodynamic and transport properties of individual species,” NASA, Tech. Rep. NASA-TM-4513, Oct. 1993. [Online]. Available: <https://ntrs.nasa.gov/citations/19940013151>
- [45] M. Rachner, “Die Stoffeigenschaften von Kerosin Jet A-1,” *DLR-Mitteilungen 98-01*, no. 1, 1998. [Online]. Available: <https://elib.dlr.de/3185/>

- [46] S. S. Vasu, D. F. Davidson, and R. K. Hanson, “Jet fuel ignition delay times: Shock tube experiments over wide conditions and surrogate model predictions,” *Combustion and Flame*, vol. 152, no. 1-2, pp. 125–143, Jan. 2008. [Online]. Available: <https://linkinghub.elsevier.com/retrieve/pii/S0010218007002313>
- [47] H. Wang, Y. Ra, M. Jia, and R. D. Reitz, “Development of a reduced n-dodecane-PAH mechanism and its application for n-dodecane soot predictions,” *Fuel*, vol. 136, pp. 25–36, Nov. 2014. [Online]. Available: <https://www.sciencedirect.com/science/article/pii/S0016236114006784>
- [48] H. Ogawa, “Physical Insight into Fuel-Air Mixing for Upstream-Fuel-Injected Scramjets via Multi-Objective Design Optimization,” *Journal of Propulsion and Power*, vol. 31, no. 6, pp. 1505–1523, Nov. 2015. [Online]. Available: <https://arc.aiaa.org/doi/10.2514/1.B35661>
- [49] K. Ma, Z. Zhang, Y. Liu, and Z. Jiang, “Aerodynamic principles of shock-induced combustion ramjet engines,” *Aerospace Science and Technology*, vol. 103, p. 105901, Aug. 2020. [Online]. Available: <https://linkinghub.elsevier.com/retrieve/pii/S1270963820305836>

Appendix A

Properties of Jet-A and Reaction Mechanism

Chemical reactions for Jet-A aviation fuel is modelled using the generalized hydrocarbon mechanism of Jachimowski [42], thermodynamic relations are from Gordon and McBride [44]. Equations (5.9) through (5.12), defined by Jachimowski for the generalized hydrocarbon mechanism, are used to calculate equilibrium constants using equation (3.37). Reverse reaction rates are then obtained and fit to the Arrhenius rate equation:

$$k = AT^\beta \exp\left(\frac{E_a}{RT}\right) \quad (\text{A.1})$$

The $\overline{\text{CH}}$ decomposition reaction rate was found by Jachimowski [42] to be pressure dependant, but since this feature does not exist in hy2Foam yet, rates were taken at a representative pressure of 3 atm. The forward and reverse rate constants used in this report are given in table A.1.

Specific heat capacities, per mass, for radicals were calculated similar to how enthalpy and entropy were obtained, that is:

$$c_v(\overline{\text{CH}_2}) = c_v(\text{Jet-A}) \quad (\text{A.2})$$

$$c_v(\overline{\text{CH}}) = c_v(\overline{\text{CH}_2}) + c_v(\text{C}_3\text{H}_7) - c_v(\text{C}_3\text{H}_8) \quad (\text{A.3})$$

$$c_v(\overline{\text{C}}) = c_v(\overline{\text{CH}}) + c_v(\text{C}_3\text{H}_6) - c_v(\text{C}_3\text{H}_7) \quad (\text{A.4})$$

Currently, hy2Foam only accepts heat capacities given in the form obtained from statistical mechanics, found by differentiating equation (3.21) with respect to temperature. The heat capacity, divided by the specific gas constant, and neglecting electronic energies is [16]:

$$\frac{c_{v,s}}{R_s} = n_{\text{trans}} + n_{\text{rot}} + \sum_i g_{i,\text{vib}} \frac{(\theta_{i,\text{vib}}/T)^2 \exp(\theta_{i,\text{vib}}/T)}{(\exp(\theta_{i,\text{vib}}/T) - 1)^2} \quad (\text{A.5})$$

where n_{trans} and n_{rot} are coefficients for translational and rotational energies, respectively. Physically, $n_{\text{trans}} = 1.5$ and $n_{\text{rot}} = 0, 1$ or 1.5 depending on molecular geometry, but for this purpose they do not have to correspond to anything physical. Parameters for equation (A.5) are given in table A.2 along with the chemical potential, or heat of formation, in terms of the gas constant. It is interesting to note that the best fit curve for Jet-A, commonly modelled as $\text{C}_{12}\text{H}_{23}$, has 100 vibrational modes which is close to the physical number of 99 modes. No attempt was made to enforce a certain number of vibrational modes. A nonlinear molecule has $3N - 6$ vibrational modes, where N is the number of atoms.

Viscosity and thermal conductivity data for Jet-A are taken from Rachner [45] and fit to CEA curves, shown in equation (3.14) with coefficients in table A.3. Transport properties for the abstracted radicals, $\overline{\text{CH}_2}$, $\overline{\text{CH}}$ and $\overline{\text{C}}$, were assumed to be the same as Jet-A.

Table A.1: Reaction data for generalized hydrocarbon mechanism for Jet-A.

| Reaction | Forward Rates | | | Reverse Rates | | |
|---|-----------------------|---------|---------------|-----------------------|---------|---------------|
| | A^1 | β | E_a [J/mol] | A^1 | β | E_a [J/mol] |
| $O_2 + \overline{CH_2} \rightleftharpoons HO_2 + \overline{CH}$ | 1.33×10^{10} | 0.0 | 217567.9 | 4.28×10^{11} | -0.9 | 146597.3 |
| $H + \overline{CH_2} \rightleftharpoons H_2 + \overline{CH}$ | 5.40×10^{10} | 0.0 | 32216.9 | 1.74×10^{11} | -0.5 | 189299.5 |
| $O + \overline{CH_2} \rightleftharpoons OH + \overline{CH}$ | 4.25×10^{10} | 0.0 | 40584.6 | 6.47×10^{10} | -0.5 | 189477.5 |
| $OH + \overline{CH_2} \rightleftharpoons H_2O + \overline{CH}$ | 3.26×10^1 | 2.75 | -3246.8 | 5.94×10^3 | 1.9 | 220260.1 |
| $O_2 + \overline{CH} \rightleftharpoons HO_2 + \overline{C}$ | 1.50×10^8 | 0.0 | 20920.0 | 8.24×10^{10} | -1.1 | 39939.4 |
| $HO_2 + aCH_2 \rightleftharpoons H_2O_2 + aCH$ | 2.50×10^8 | 0.0 | 43932.0 | 7.70×10^{10} | -1.0 | 132831.9 |
| $\overline{CH} \rightleftharpoons H + \overline{C}^2$ | 7.65×10^{11} | 0.0 | 132323.0 | 3.60×10^9 | -0.5 | -57889.4 |
| $OH + \overline{C} \rightleftharpoons CO + H$ | 1.00×10^9 | 0.0 | 0.0 | 1.16×10^{-5} | 3.0 | -69374.2 |
| $CO + OH \rightleftharpoons CO_2 + H$ | 1.68×10^4 | 1.3 | -2744.6 | 3.15×10^{10} | 0.2 | 105464.0 |
| $CO + O + M \rightleftharpoons CO_2 + M$ | 2.50×10^9 | 0.0 | 18284.3 | 2.58×10^{19} | -1.3 | 555588.2 |
| $CO + HO_2 \rightleftharpoons CO_2 + OH$ | 1.00×10^8 | 0.0 | 41840.0 | 5.27×10^{10} | -0.4 | 298556.6 |
| $H + O_2 \rightleftharpoons O + OH$ | 1.42×10^{11} | 0.0 | 68617.6 | 3.60×10^8 | 0.4 | -3739.8 |
| $H_2 + OH \rightleftharpoons H + H_2O$ | 3.16×10^4 | 1.8 | 12677.9 | 1.59×10^6 | 1.5 | 78994.9 |
| $H_2 + O \rightleftharpoons H + OH$ | 2.07×10^{11} | 0.0 | 57530.3 | 1.32×10^{11} | -0.0 | 49698.0 |
| $2OH \rightleftharpoons H_2O + O$ | 5.50×10^{10} | 0.0 | 29287.7 | 4.33×10^{12} | -0.3 | 103436.9 |
| $H + OH + M \rightleftharpoons H_2O + M$ | 2.21×10^{16} | -2.0 | 0.0 | 1.46×10^{22} | -2.4 | 503709.3 |
| $2H + M \rightleftharpoons H_2 + M$ | 6.53×10^{11} | -1.0 | 0.0 | 7.61×10^{15} | -1.1 | 437285.0 |
| $H + O_2 + M \rightleftharpoons HO_2 + M$ | 3.20×10^{12} | -1.0 | 0.0 | 3.73×10^{17} | -1.6 | 209231.8 |
| $HO_2 + OH \rightleftharpoons H_2O + O_2$ | 5.00×10^{10} | 0.0 | 4183.8 | 2.83×10^{11} | 0.1 | 298661.3 |
| $H + HO_2 \rightleftharpoons H_2 + O_2$ | 2.53×10^{10} | 0.0 | 2929.2 | 2.53×10^9 | 0.4 | 230982.4 |
| $H + HO_2 \rightleftharpoons 2OH$ | 1.99×10^{11} | 0.0 | 7531.2 | 2.35×10^7 | 0.8 | 154998.2 |
| $HO_2 + O \rightleftharpoons O_2 + OH$ | 5.00×10^{10} | 0.0 | 4183.8 | 2.33×10^9 | 0.4 | 224008.3 |
| $2HO_2 \rightleftharpoons H_2O_2 + O_2$ | 1.99×10^9 | 0.0 | 0.0 | 3.39×10^{10} | -0.1 | 160530.7 |
| $H_2 + HO_2 \rightleftharpoons H + H_2O_2$ | 3.01×10^8 | 0.0 | 78240.8 | 7.02×10^{10} | -0.6 | 11114.8 |
| $H_2O_2 + OH \rightleftharpoons H_2O + HO_2$ | 1.02×10^{10} | 0.0 | 7949.5 | 2.20×10^9 | 0.3 | 141392.4 |
| $H_2O_2 + M \rightleftharpoons 2OH + M$ | 1.21×10^{14} | 0.0 | 190372.1 | 2.70×10^4 | 1.3 | -30416.0 |

¹ Units are in s, kmol and m³² Rate constants are computed at 3 atm

Table A.2: Parameters for heat capacity.

| Species | n_{trans} | n_{rot} | $g_{i,vib}$ | $\theta_{i,vib}$ [K] | h_s°/R_s [K] |
|-------------------|-------------|-----------|-------------|----------------------|---------------------|
| Jet-A | 1.5 | 1.5 | 35 | 2195 | -30029 |
| | | | 44 | 644 | |
| | | | 21 | 3890 | |
| $\overline{CH_2}$ | 1.0 | 0.7 | 3 | 3261 | -2518 |
| | | | 3 | 1592 | |
| \overline{CH} | 1.0 | 0.4 | 3 | 1588 | 5032 |
| | | | 2 | 3612 | |
| \overline{C} | 1.0 | 0.3 | 2 | 3250 | 1949 |
| | | | 2 | 1721 | |

Table A.3: CEA coefficients for Jet-A, $\overline{\text{CH}_2}$, $\overline{\text{CH}}$ and $\overline{\text{C}}$.

| | μ | κ |
|-----|---------------------------------|---------------------------------|
| A | $-4.344\,688\,5 \times 10^{-2}$ | $-2.111\,179\,9 \times 10^{-1}$ |
| B | $-1.138\,785\,9 \times 10^5$ | $-1.964\,815\,1 \times 10^3$ |
| C | $1.134\,767\,4 \times 10^5$ | $2.131\,600\,6 \times 10^5$ |
| D | $6.778\,469\,8$ | $1.011\,371\,9 \times 10^1$ |

Appendix B

Steady State Convergence

CFD residuals, the imbalance between both sides of the discretized equation, are used to assess the time accuracy of a solution. In OpenFoam, these are represented by the normalized residual, defined as:

$$r = \frac{\sum |\mathbf{A}\bar{\mathbf{x}} - \mathbf{b}|}{\sum |\mathbf{A}\bar{\mathbf{x}} - \mathbf{b}| + |\mathbf{A}\mathbf{x} - \mathbf{A}\bar{\mathbf{x}}|} \quad (\text{B.1})$$

While only steady state behaviour is studied in this report, residuals are monitored to determine how well quantities are conserved. To verify that steady state was reached, relevant flow quantities were evaluated at for each recorded time-step. For the under-expanded jet, the measured quantities were distance to first shock and pre-shock static pressure, shown in figure B.1 along with residuals. Steady state convergence for the turbulent hydrogen mixing study is evaluated using total pressure and hydrogen mass fraction at $x/D = 5.51$ and at the jet diameter. This is shown, along with residuals, in figure B.2. Mixing efficiencies for the Yang et al. case are evaluated on either side of the THTJ, $x = 620$ mm and $x = 720$ mm, shown with residuals in figures B.3 through B.4. For the reacting case, shown in figure B.5, static pressure along the centre-line was used instead. In figure B.3, only part of the time data is shown due to a minor error in recording the time data which was resolved. However, the data still shows low residuals and steady state convergence. To aid in visualization, quantities in these graphs have been normalized by their final values and a shaded band highlighting $\pm 1\%$ of the final value is shown.

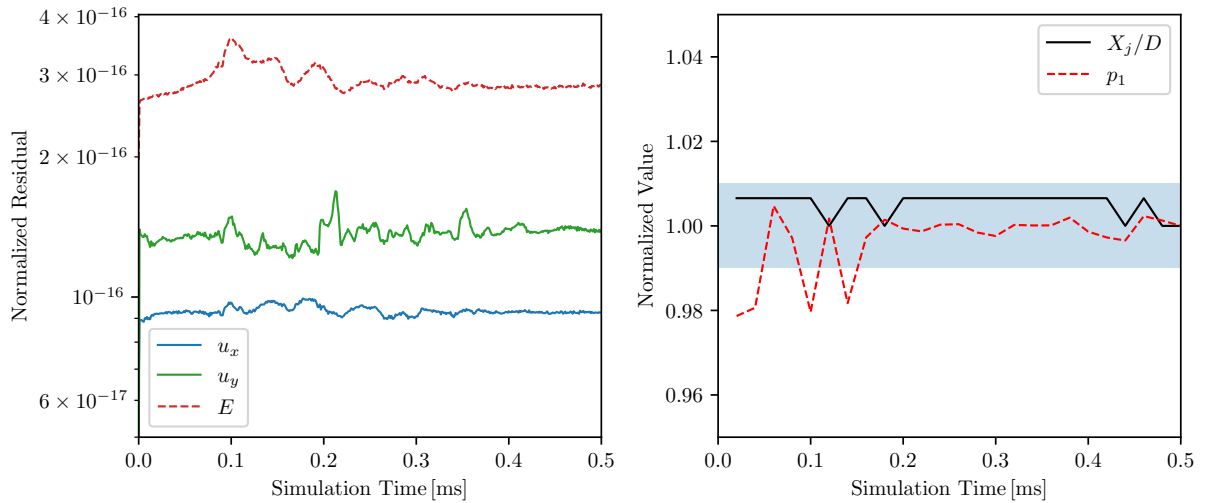


Figure B.1: Residuals for velocity and energy equations (left) and time data (right) for under-expanded jet simulation. Shaded band highlights $\pm 1\%$ of final value.

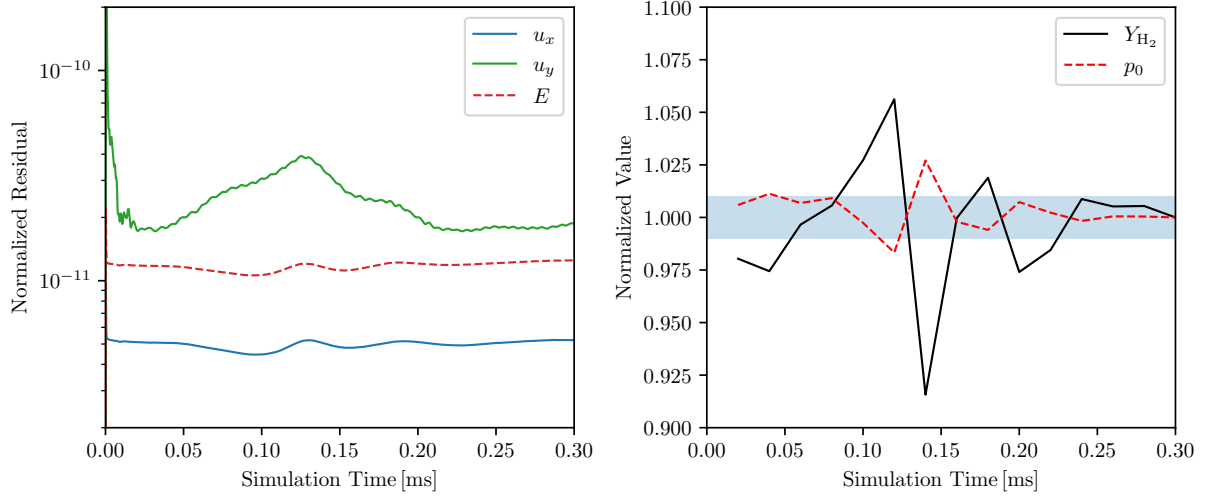


Figure B.2: Residuals for velocity and energy equations (left) and time data (right) for turbulent mixing simulation. Total pressure and hydrogen mass fraction taken at $x/D = 5.51$ and $r = D/2$. Shaded band highlights $\pm 1\%$ of final value.

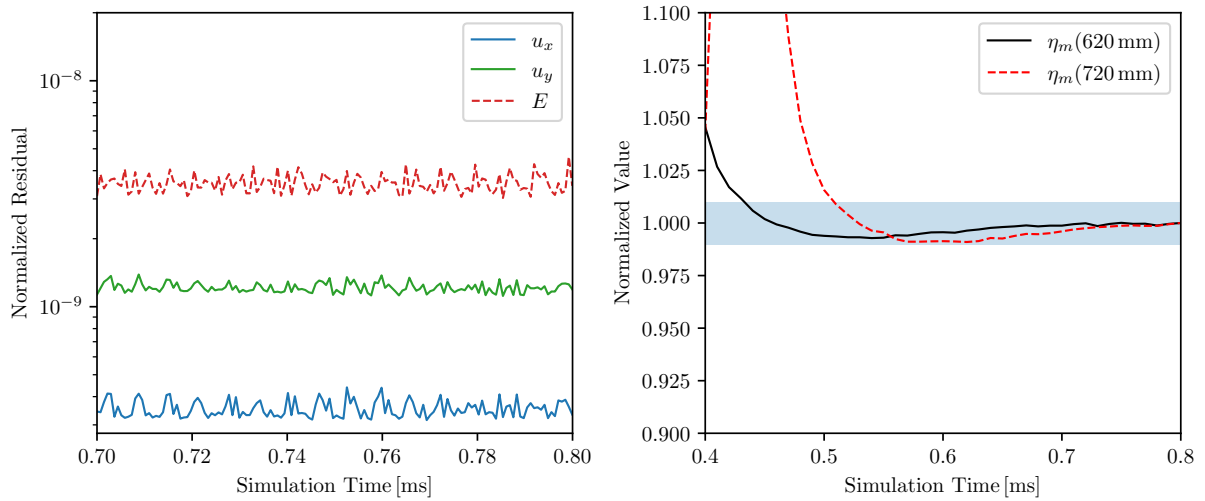


Figure B.3: Residuals for velocity and energy equations (left) and time data (right) for Yang et al. frozen simulation with only the strut enabled. Shaded band highlights $\pm 1\%$ of final value.

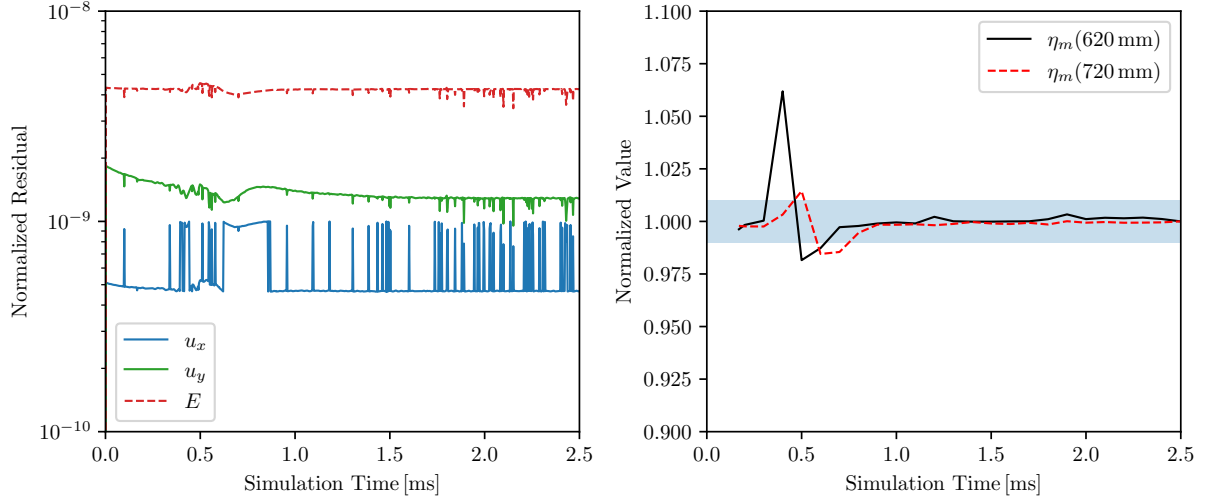


Figure B.4: Residuals for velocity and energy equations (left) and time data (right) for Yang et al. frozen simulation with strut and THTJ. Shaded band highlights $\pm 1\%$ of final value.

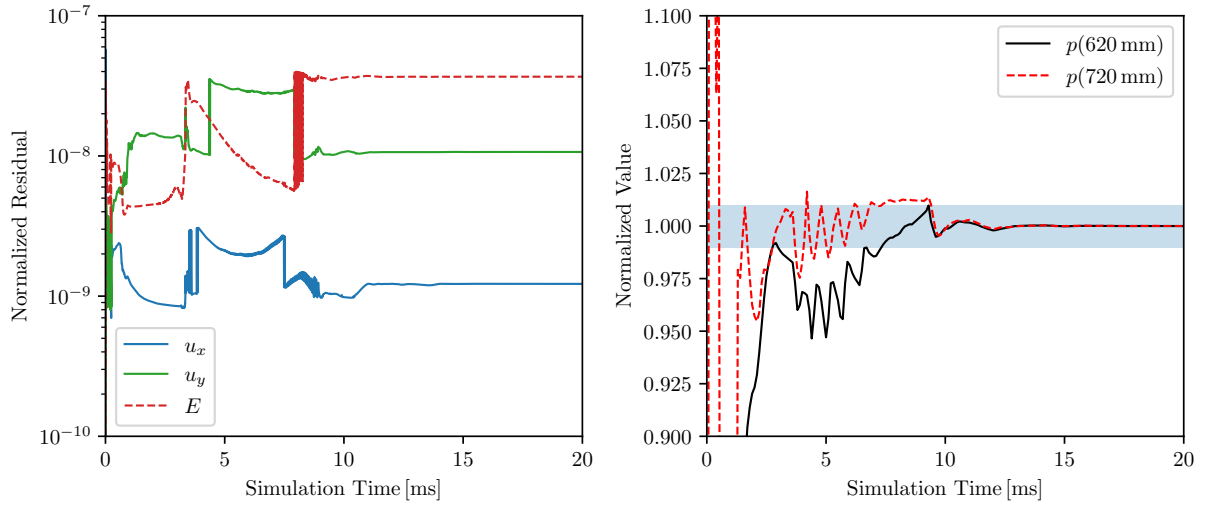


Figure B.5: Residuals for velocity and energy equations (left) and time data (right) for Yang et al. reacting simulation. Shaded band highlights $\pm 1\%$ of final value.